Laboratory of Advanced Energy Systems
Department of Engineering Physics and Mathematics
Helsinki University of Technology
FIN-02015 HUT, Finland

NUCLEAR DIAGNOSTICS IN THE STUDY OF RELATIVISTIC LASER-PLASMA INTERACTIONS

Marko Santala

Dissertation for the degree of Doctor of Technology to be presented with due permission for public examination and debate in Auditorium F1 at Helsinki University of Technology (Espoo, Finland) on the 4th June, 2001 at 12 o'clock noon.

Espoo 2001

ISBN 951-22-5481-6

Otamedia Oy
Espoo 2001

Abstract

Laser intensities available for experiments on laser-plasma interactions have increased rapidly during the past decade. Today, intensity in the range 10^{19}—10^{20} W/cm^2 is commonly available. These intensities result in fully relativistic electron motion and effective temperature in the MeV range. It is of great interest to characterise the properties of the fast particles, electrons and ions, emerging from the laser-plasma interaction. However, many of the techniques previously applied when particles energies reached only tens or hundreds of keV have proven insufficient at the highest intensities.

In this thesis, nuclear activation techniques have been developed for the study of the fast particles in laser-plasma experiments. These techniques have been applied in experiments carried out at the 50 TW VULCAN laser at Rutherford Appleton Laboratory. Simple nuclear reactions typically have reaction thresholds from a few MeV to tens of MeV. Hence, such reactions have two important properties: they provide energy sensitivity in the presently interesting energy range and they are completely insensitive to particles of low energy, removing the potential ambiguity between detecting many low-energy particles vs. a single energetic one.

For the detection of fast electrons, photonuclear reactions have been applied. This is an indirect process where the electrons first generate bremsstrahlung photons which subsequently induce activation in the detector materials. The reaction products are often positron-emitting. This allows sensitive detection of the induced activity by coincidence techniques. In laser-solid experiments, the photonuclear activation has been applied to get information on the angular distribution of the fastest electrons. In plasma accelerator experiments, the technique has been applied for the study of electron angular distribution, temperature and total yield. It has been shown that the electron spectrum is produced by plasma accelerator experiment is nearly an order of magnitude hotter than in laser-solid experiments at similar laser intensity.

Fast protons from the laser-solid interactions have been characterised by proton-induced reactions. Such reactions commonly produce positron-emitting products allowing the detection by coindicence techniques. Because of the continuous slowing-down and the short range of protons, spectral measurements could be carried out by using stacked foil detectors. With thin targets, these measurements showed that a much harder proton spectrum is generally observed behind the target than in the plasma blow-off direction. Nuclear reactions induced by heavier ions like ^{12}C in the plasma blow-off were also detected in this work.

Preface

The work summarised in this thesis has been carried out in the Laboratory of Advanced Energy Systems in the Helsinki University of Technology and in the Plasma Physics Group in the Imperial College.

I would like to express my deep gratitude to prof. R. Salomaa, my supervisor, for guidance in the multi-faceted field of laser-matter interactions. I am particularly grateful to prof. T. Bell for inviting me to the Imperial College, where the experimental work in this thesis was carried out.

I would like to thank Mr. B. Dangor, Dr. K. Krushelnick, Dr. Z. Najmudin and Dr. M. Zepf for close guiding in the planning and execution of the experimental work and the analysis of the results. I am also obliged to everybody in the experimental groups I worked with as well as the laser support people at the Rutherford Appleton Laboratory. I also would like to express special thanks to everybody in the laboratory 'Miilu', the people in the Laboratory of Advanced Energy Systems and in the Plasma Physics Group for invaluable advice and discussions as well as all the memorable moments of working together.

I am obliged to all the sources of funding that made this work possible. I would like to thank the graduate schools of the Academy of Finland for the core funding. I would like to acknowledge the crucial role of the European Union TMR network SILASI for funding my visit to Imperial College. I also would like to thank Jenny ja Antti Wihurin Rahasto for providing additional funding for my thesis.

Marko Santala

Original publications

I. P. A. Norreys, M. Santala, E. Clark, M. Zepf, I. Watts, F. N. Beg, K. Krushelnick, M. Tatarakis, A. E. Dangor, X. Fang, P. Graham, T. McCanny, R. P. Singhal, K. W. D. Ledingham, A. Creswell, D. C. W. Sanderson, J. Magill, A. Machacek, J. S. Wark, R. Allott, B. Kennedy, and D. Neely. *Observation of a highly directional gamma-ray beam from ultra-short, ultra-intense laser pulse interactions with solids.* Phys. Plasmas **6**, 2150–2156 (1999).

II. M. I. K. Santala, E. Clark, I. Watts, F. N. Beg, M. Tatarakis, M. Zepf, K. Krushelnick, A. E. Dangor, T. McCanny, I. Spencer, R. P. Singhal, K. W. D. Ledingham, S. C. Wilks, A. C. Machacek, J. S. Wark, R. Allott, R. J. Clarke, P. A. Norreys. *The effect of the plasma density scale-length on the direction of fast electrons in relativistic laser-solid interactions.* Phys. Rev. Lett. **84** 1459–1462 (2000).

III. K. W. D. Ledingham, I. Spencer, T. McCanny, R. P. Singhal, M. I. K. Santala, E. Clark, I. Watts, F. N. Beg, M. Zepf, K. Krushelnick, M. Tatarakis, A. E. Dangor, P. A. Norreys, R. Allot, D. Neely, R. J. Clarke, A. Machachek, J. S. Wark, A. J. Cresswell, D. C. W. Sanderson, and J. Magill. *Photonuclear physics when a multiterawatt laser pulse interacts with solid targets.* Phys. Rev. Lett. **84** 899–902 (2000).

IV. M. I. K. Santala, E. Clark, I. Watts, F. N. Beg, M. Tatarakis, M. Zepf, K. Krushelnick, A. E. Dangor, T. McCanny, I. Spencer, K. W. D. Ledingham, A. C. Machacek, J. S. Wark, R. Allott, R. J. Clarke, P. A. Norreys. *Fast-ion induced nuclear reactions in the plasma blow-off in intense laser-solid interactions.* Inertial Fusion Sciences and Applications 99 Conference, 12-17 September 1999, Bordeaux, France. Edited by C. Labaune *et al.* Elsevier, Paris, p. 1016–1019 (2000).

V. M. I. K. Santala , M. Zepf, F. N. Beg, E. L. Clark , A. E. Dangor, K. Krushelnick, M. Tatarakis, I. Watts, K. W. D. Ledingham, T. McCanny, I. Spencer, A. C. Machacek, R. Allott, and R. J. Clarke. *Production of radioactive nuclides by energetic protons generated from intense laser-plasma interactions.* Appl. Phys. Lett. **78** 19–21 (2001).

VI. M. I. K. Santala, Z. Najmudin, E. L. Clark, M. Tatarakis, K. Krushelnick, A. E. Dangor, V. Malka, J. Faure, R. Allott, and R. J. Clarke. *Observation of a hot high-current electron beam from a self-modulated laser wakefield accelerator.* Phys. Rev. Lett. **86** 1227–1230 (2001).

All the publications selected for this dissertation have more than one author because the scientific work described in them represents efforts of large collaborations. However, in the selected publications the author has had a key role in the design and implementation of the nuclear diagnostics described therein. The author has also carried out the main parts of the analysis of the related experimental data, except for Publ. III where prof. Ledingham's group has substantially contributed in the analysis.

Contents

CHAPTER 1

Introduction

Ever since lasers were invented [1] intense efforts have been concentrated on developing pulsed lasers with high instantaneous power. Thanks to the close-to-ideal optical properties of laser beams the effects of this high power can be further increased tremendously by focussing optics resulting in an extremely high light intensity. To match the highest intensities achievable in laboratory presently, approximately 10^{20} W/cm^2 [2, 3], all the power incident on Earth from Sun ($\approx 10^{17}$ W) would need to be directed to a spot with 0.5 mm diameter. The study of the interaction between light and matter at such extreme conditions presents formidable technological and theoretical challenges.

A high power laser system consists of a low-power oscillator and one or more amplifiers. The oscillator determines the spectral and temporal characteristics of the laser pulse, and amplifiers increase the pulse energy to the desired level. Because of non-linear material properties and potential for optical damage the beam diameter must be gradually increased as the pulse energy increases. This increases sharply the cost of the laser system. To reach high powers, one has traditionally resorted to the use of multiple relatively small beamlines. Most high-power lasers have been constructed for the study of inertial confinement fusion (ICF). Some examples of this path are the present VULCAN (8 beams) [4], NOVA (10 beams) [5] and GEKKO-XII (12 beams) [6, 7] lasers, and the forthcoming NIF (192 beams) [5, 8] and MÉGAJOULE (240 beams) [9] projects.

As the beam-size largely depends on laser power, the conventional amplifying of the ever-shorter pulses available from modern laser oscillators [10] is prohibitively expensive. In the late 1980's a novel approach, *chirped-pulse amplification* (CPA) for high-power generation was discovered [2, 11]. The idea (see Fig. 1.1) is to stretch a low-power femtosecond pulse, amplify the stretched pulse, and finally recompress the amplified pulse back to a short pulselength. As the pulse-length is large in the amplifiers, the power remains moderate. Only the few optical components necessary after recompression need to withstand the pulses at the ultimate power.

Typically, the compression gratings are damaged most easily, and hence, the size of the gratings mainly determines the achievable pulse energy. After focusing the intensity in the beam quickly exceeds the damage threshold of all optical materials. Hence, the final optical components and the target must be placed in vacuum. At focus, the intensity of an ultra-intense laser beam commonly reaches 10^{18} W/cm^2—10^{20} W/cm^2. Such intensity results in an instantaneous ionisation of the target material and in plasma formation. Free electrons in the plasma reach relativistic energies from the motion in the electro-magnetic field of laser light alone, hence, the plasma must be treated relativistically. Through complex interaction mechanisms electrons may gain up to 100 MeV of energy. As the electrons are partly expelled from the regions of the highest intensity, large space-charge fields set the ions in motion as well.

As the final outcome of the laser-plasma interaction, intense jets of electrons and

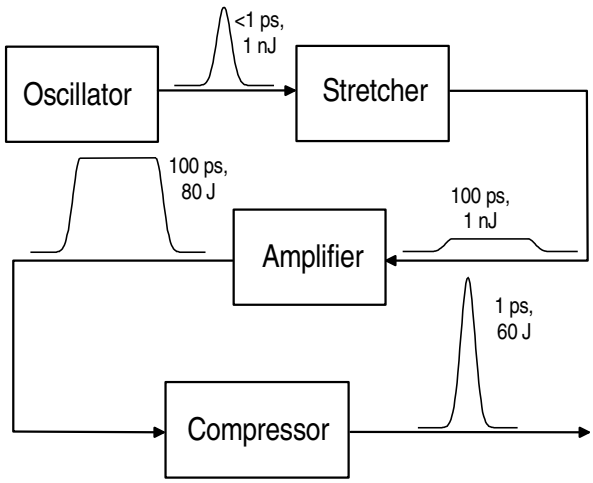

FIGURE 1.1. *The principle of* CPA *amplification: A low power, femtosecond pulse from the oscillator* OSC *is stretched by dispersive stretcher. This is amplified yielding a pulse with large energy but low power. In compressor, the dispersion introduced in stretcher is exactly cancelled resulting in a high-power short pulse.*

ions at energies of many MeVs emerge from the interaction zone, in addition to reflected, scattered and spectrally modulated laser light. Characterising these is of utmost importance for the understanding of the laser-plasma interactions. No conventional diagnostics can survive in the hot, high-pressure environment of these interactions. Therefore, analysing the outcome of the interaction is the only experimental way to find out about the important processes during the interaction itself.

In this thesis, the intense particle jets produced by the laser-plasma interactions are studied through radioactivity induced by the energetic particles. Two main groups of reactions have been applied: photonuclear reactions to study the fast electrons and ion-induced reactions to study the fast ions. These methods have been applied in two different classes of laser-plasma experiments: laser-solid experiments where the laser beam interacts with an inhomogeneous, very dense (up to solid density) plasma and plasma accelerator experiments where the laser beam is channelled through fairly low-density, homogeneous plasma. The former interaction can be extremely abrupt as the propagation of the laser beam is suddenly prohibited over a distance that can be less than the laser wavelength. In the latter, the ultra-intense laser-plasma interaction can prevail over a millimetre-scale distance.

The present thesis is based on experimental work carried out on the VULCAN laser at the Rutherford Appleton Laboratories (RAL). It is a laser capable of producing up to 50 J energy on target in 1 ps and the laser beam can be focussed to a spot with peak intensity exceeding 10^{19} W/cm^2 [12]. Even though this work has been carried out at a large laser installation the results should be relevant to a much broader base of lasers. The rapid development of lasers producing ultra-short pulses [10] and amplifiers for them [13, 14, 15] allow much smaller table-top laser systems attain similar focussed intensity. Hence, similar experimental conditions could be studied by much smaller facilities.

This thesis is organised as follows: Chapter 2 discusses some of the basic concepts of intense laser-plasma interactions. Chapter 3 describes the laser-solid interactions and the study of the fast electrons by photonuclear reactions. Chapter 4 discusses the detection of fast ions – protons and heavier ions – by ion-induced activation techniques. In Chapter 5 the study of plasma accelerators by photonuclear techniques is presented. Finally, in Chapter 6 the main findings and achievements of this thesis work are summarised.

The experimental work in this thesis has been carried out in the Plasma Physics Group of the Imperial College, London. The stay with Imperial College was supported by an European Union TMR network SILASI (Super-Intense LAser-Solid Interactions, Grant No. ERBFMRX-CT96-0043).

CHAPTER 2

Physics in laser-plasma interaction

A great variety of physical phenomena results from the tight coupling between the electromagnetic field of the laser light, the fields created by plasma disturbances and how these affect the motion of the plasma particles. In this chapter, some plasma concepts important to phenomena in ultra-intense laser-plasma interactions are briefly presented. For more detailed presentation the reader is referred to textbooks on general plasma physics (*e.g.* by Chen [16]) and on laser-plasma interaction (*e.g.* by Kruer [17]) as well as review articles on phenomena at very high intensities (*e.g.* by Esarey [18] and Wilks [19]).

2.1 Plasma frequency

Plasmas are quasi-neutral fluids consisting of free electrons and wholly or partially ionised ions. A fundamental property of plasma is its tendency to maintain this quasi-neutrality. Any disturbance results in the build-up of fields opposing it. The initial plasma response is usually mediated through the motion of the electrons due to the great mass difference between the electrons and ions. During fast ($<$ 1 ps) laser-plasma interactions the ions can usually be treated as immobile except at the very highest intensities. However, their motion is important in the later evolution of the plasma.

If the electrons in plasma are displaced from their equilibrium position the restoring electric field proportional to the displacement and the electron density is produced. If electrons can move freely after the initial disturbance an electrostatic oscillation at a frequency ω_p dependent on the electron density n_e results:

$$\omega_p^2 = \frac{n_e e^2}{\epsilon_0 m_e} \tag{2.1}$$

This frequency is called the (electron) plasma frequency. It is a very important plasma characteristic as it describes the fastest timescale at which plasma responds to disturbances. For the propagation of electromagnetic (EM) waves (*e.g.* light) in plasma, the plasma frequency represents the lowest EM wave frequency (ω) that can propagate through plasma. If ($\omega > \omega_p$) the EM wave can propagate in plasma and plasma is called *underdense*. If $\omega < \omega_p$ the EM wave propagation is prohibited (electron motion 'short-circuits' the EM field) and plasma is called *overdense*. The density, where $\omega = \omega_p$ is defined as the *critical density* n_c.

In laser-plasma experiments, underdense plasma only is present in typical gasjet experiments. In laser-solid experiments, the presence of the critical density surface is of prime importance. Due to the pre-ionisation of the surface that commonly occurs, there is also inhomogeneous underdense plasma present in front of the critical density. The region beyond this can be highly overdense, and consequently, is effectively shielded from the laser fields.

In ultra-intense laser-plasma interactions the electron kinetic energy can exceed the rest mass of electrons. The plasma frequency must then be corrected for rel-

ativistic mass increase. The electron mass m_e has to be replaced by γm_e, where $\gamma = (1-(v/c)^2)^{-1/2}$. Consequently, the plasma frequency of the relativistic plasma is lower and the critical density higher than that of non-relativistic case. At a given light frequency, it is possible that light can propagate in plasma that would be overdense without relativistic corrections.

2.2 Quiver motion

The electromagnetic fields of light consist of transverse electric and magnetic fields that are perpendicular to each other. Electrons in such fields begin to oscillate at the light frequency. This is called the quiver motion of the electrons. The electric field dominates this motion at low intensities as the force excerted by the magnetic field is lower by factor v/c. In linear-polarised light the oscillation is thus linear and transverse to the direction of light propagation. At high intensity, with v approaching c, the magnetic field becomes also important, and the electron trajectories turn into 'figure-8' shape.

It can be shown that the transverse momentum of an electron $p_\perp = eA$ where A is the peak vector potential of the electromagnetic field (with $\mathbf{E} = -\partial\mathbf{A}/\partial t$ and $\mathbf{B} = \nabla \times \mathbf{A}$). It is seen that $A \propto E/\omega$. At intensity I the peak value of vector potential, A, can be calculated from relation

$$A^2 = \frac{2I}{\epsilon_0 c \omega^2}. \tag{2.2}$$

The normalized transverse momentum a_0 is defined as

$$a_0 = \frac{eA}{m_e c}. \tag{2.3}$$

This is a measure of how significant the relativistic effects are. At large intensities ($v \approx c$) the magnetic force cannot be ignored anymore. It results in a velocity component in longitudinal direction, with frequencies 0 and 2ω. The normalised momentum in this motion $a_x = a_0^2/2$. If the electron was initially at rest and there are no other forces acting on the electron this results in a net transport of electrons in the direction of the light propagation with a speed modulated at the frequency 2ω. The leading edge of a laser pulse sets the electron in motion and the trailing edge stops it.

It can be further shown that the total kinetic energy electron achieves due to the light fields W_{osc} is

$$W_{\mathrm{osc}} = m_e c^2(\gamma - 1) = m_e c^2 \frac{a_0^2}{2} \tag{2.4}$$

This increases linearly with the light intensity. For an electron in a 10^{19} W/cm^2 laser field at 1 μm wavelength W_{osc} is 1.87 MeV. It should be noted that the spatial extent of electron orbit then approaches 0.5 μm. If there are significant gradients on such scale or the electron density is so large that the motion leads to large space charge forces the simple picture is likely to break down.

Much of the laser-plasma interaction physics scales with a_0^2. For a given intensity this scales as λ^2. As experiments are carried out using lasers with λ ranging from 0.25 to 10 μm it is a common practise to express intensity 'normalised' to 1 μm wavelength by using units 1 Wμm^2/cm^2.

2.3 Ponderomotive force

The quiver motion described in the previous section explains electron motion in a uniform laser field. If there are gradients in the field amplitude the picture is changed. The electrons do not experience a uniform sinusoidal field all over their orbit but the field amplitude changes along it. This results in a non-linear effect called the ponderomotive force ($\mathbf{f}_{\mathrm{nl}}$) that tends to expel electrons from the regions of strong field. Averaged over an oscillation it is given by the equation

$$\langle \mathbf{f}_{\mathrm{nl}} \rangle = -\frac{e^2}{2m_e\omega^2} \nabla \left\langle E^2 \right\rangle , \tag{2.5}$$

where E is the oscillating electric field of light. The ponderomotive force closely corresponds to the light pressure.

Ponderomotive force acts mainly on the electrons, as it is dependent on the spatial extent of the particle orbits. Consequently, it tends to create charge separation and hence produces an electrostatic disturbance in the plasma. Its non-linear nature leads to an efficient coupling of different oscillations in plasma. Ponderomotive force can couple the electro-magnetic oscillations of light to the electro-static plasma waves (see the next section), which is of great importance for plasma accelerators.

The ponderomotive force is modified at relativistic intensities due to the mass increase of electrons. m_e in Eq. 2.5 must be replaced by $\langle\gamma\rangle\, m_e$ where the Lorentz factor γ is averaged over the electron orbit. The mass increase limits the electron excursion and this leads to a weakening of the ponderomotive force.

2.4 Electron acceleration by electrostatic waves in plasma

In cold plasma the electrostatic plasma oscillations (Sec. 2.1) do not propagate and only oscillation at frequency ω_p is possible. In warm plasma, however, propagating modes obeying the dispersion relation [17]

$$\omega^2 = \omega_p^2 + 3k^2 v_{th}^2 \tag{2.6}$$

are found. Here ω and k are the frequency and wave-vector associated with the wave and v_{th} is the thermal velocity of electrons.

The electric field of an electrostatic wave is parallel to the direction of propagation of the wave. Furthermore, there exist solutions to the dispersion relation (2.6) with the phase velocity ω/k close to c. Hence, relativistic electrons can co-propagate with such waves and experience a quasi-static accelerating field over a long distance. The maximum field strength of an electrostatic wave scales as $n_e^{1/2}$ and can be very large: *e.g.* at $n_e = 10^{18}$ cm^{-3} up to 100 GV/m [18].

It turns out that for forward Raman scattering (RFS), the frequency and wave vector matching conditions occur with electrostatic waves having phase velocity close to c if the laser frequency is much larger than the plasma frequency. Hence, such waves can be efficiently driven to the maximal field strength through RFS [17, 18]. The efficiency of this process is a result of the non-linear mixing of the electromagnetic laser field and the electrostatic plasma-wave through the ponderomotive force. This is the fundamental mechanism behind the self-modulated laser wakefield accelerator concept (see Ch. 5).

CHAPTER 3

Electrons in laser-solid experiments

Laser-solid interaction at intensities reaching 10^{20} W/cm^2 has been studied intensively both experimentally and numerically during past few years. This is largely due to the recent availability of lasers capable of producing such intensities as well as the enormous complexity of the interaction physics and its relevance for large-scale applications like inertial-confinement fusion (ICF). These studies are particularly relevant for the Fast Ignitor concept [20], *i.e.* using an intense short laser pulse to ignite a compressed fusion target. Being a previously unexplored regime of physics, the studies can also be motivated by plain curiosity.

Experiments have shown that laser-solid interaction generates large amounts of very energetic electrons [3, 21, 22, 23, 24, 25, Publ2]. Understanding the processes producing the electrons has presented enormous challenges for numerical studies but gradually a fairly detailed picture has developed, see *e.g.* Refs. [19, 26, 27, 28, 29]. The transport of large numbers of fast electrons is predicted to generate large magnetic fields that can collimate the electron beams [30, 31, 32, 33], and this has been also experimentally verified [34, 35]. Other interesting phenomena have been observed like the generation of the high-harmonics of the laser light due to the anharmonic motion of the electrons and the critical surface: coherent harmonics up to soft the X-ray regime have been observed [36, 37].

Strictly, the laser-solid interaction rarely occurs at a cold, sharp vacuum-solid interface but at a finite density profile due to pre-ionisation of the surface. Hence, the interaction takes place in non-uniform plasma with electron density spanning several orders of magnitude over a small distance. The size of the pre-plasma can radically change the interaction physics with dominant mechanisms ranging from those occurring at sharp boundaries to those appearing in homogeneous plasmas.

It is of crucial significance that at solid surfaces the plasma density exceeds the critical density. The electron density of *e.g.* fully ionised aluminium is 700 times the critical density at 1 μm wavelength. Hence, both underdense and overdense plasma regions exist. As the propagation of light into the overdense regions is not permitted the laser light will either be absorbed or reflected. This implies that the laser light excerts a large force on the particles in the plasma, setting them in motion. At intensity 10^{19} W/cm^2 the light pressure (for absorption) is 330 TPa (3.3 Gbar), exceeding the bulk modulus of metals by three orders of magnitude.

3.1 Fast electron generation mechanisms

The term 'fast electrons' generally refers to (a large number of) electrons with more kinetic energy than would be expected through simple Maxwellian distribution. Often they can be observed as long tails in the electron distribution with much higher effective temperature than for the 'bulk' electrons. Fast electrons are generally nor produced by mere plasma heating but are produced through specific acceleration mechanisms. In traditional ICF research, typical mechanisms are *e.g.* plasma waves

driven by Raman scattering, two-plasmon decay and resonance absorption [17].

In intense laser-solid interaction, fast electrons can be accelerated by several different mechanisms [19]. It has been found that nearly half of the incident laser energy can be transferred to the electrons [26, 27]. Understanding the roles of different acceleration mechanisms is essential for development of practical applications as the direction and spectrum of the accelerated electrons can depend on the mechanisms in action. It is also important to find out how the mechanisms are affected by variations in laser and plasma parameters.

3.1.1 Resonance absorption

Resonance absorption [17, 38, 39] is perhaps the most studied absorption mechanism as it is very relevant in ICF studies. In resonance absorption, p-polarised light incident in an oblique angle on plasma is partially absorbed and the energy is transferred to a resonant electrostatic plasma wave at the critical density. If the exciting field is sufficiently strong the plasma wave can reach wavebreaking resulting in production of a large number of fast electrons [40].

Efficiency of resonance absorption is strongly dependent on the angle of incidence and plasma scale-length. A large component of **E** along the surface normal enhances efficiency favouring a highly oblique angle of incidence. On the other hand, the bigger the angle of incidence the further the reflection point is from the critical surface and the weaker is the coupling between the light and the plasma wave. Under optimal conditions up to half of the incident energy can be absorbed.

The simple classical model describes the experimentally observed absorption well up to intensities up to about 10^{16} Wμm^2/cm^2 [41, 42]. Above this, the relativistic motion of electrons in the laser field has to be taken in account. Furthermore, new absorption mechanisms are introduced [19].

3.1.2 Brunel mechanism

In plasmas of a very small scale-length the Brunel mechanism [43], also called vacuum heating, can be an important mechanism. The principal idea is that electrons are dragged out of the target surface on one half of light period, get accelerated into vacuum and return as the light field reverses. It is possible for them to return to the surface with velocity close to the quiver velocity v_{osc}. As the laser fields are quickly attenuated beyond the surface, the other half of light oscillation period is not able to stop the electron. The net result is that a large number of electrons gets accelerated into the target, directly by the laser fields.

Computer simulations have shown that the Brunel mechanism produces fast electrons preferentially along the direction of the target normal [44]. Simulations also show that resonance absorption has a tendency to give to the fast electrons some momentum also along the laser **k** vector, that is the electrons would be directed more along the laser light. Hence, by measuring the angular distribution of the fast electrons one could identify the prevailing mechanisms.

3.1.3 Ponderomotive absorption

Ponderomotive absorption ($\mathbf{v} \times \mathbf{B}$ absorption, $\mathbf{j} \times \mathbf{B}$ absorption) [45] is an absorption mechanism resulting from the fact that magnetic field of the light field becomes important when the electron quiver motion becomes relativistic. The longitudinal component in the quiver motion then becomes more and more important. This results in electrons oscillating in the longitudinal direction at frequency 2ω. At critical surface the electrons can first gain energy from the light field and then be pushed across the critical surface, thus escaping from the light field. This mechanism generates a train of electron bunches with separation of $\lambda/2$ into the direction of laser propagation. The simulations in [45] predict that the electrons accelerated by this mechanism can reach effective temperatures of about 1 MeV (10^{10} K) at an intensity of 10^{19} W/cm^2 with efficiency up to 50 %. Similar results have been observed also in experiments [21, 22, 24].

3.1.4 Other mechanisms

At relativistic laser intensities other electron acceleration mechanisms can also be important. The rapid motion of large numbers of particles can generate strong quasi-static fields that can affect particle trajectories so that they experience large acceleration in the fields. An example is the $\mathbf{B}$ loop mechanism [27] where electrons may undergo several ponderomotive acceleration phases by spinning around in azimuthal magnetic field generated by the large electron current.

If the plasma scale-length is much larger than the laser wavelength, the same mechanisms acting in underdense plasma accelerators (see Chap. 5) may become important. Such mechanisms include wakefield acceleration [18, 46] and direct laser acceleration [47]. Other parametric processes may also be important.

3.2 Diagnosing fast electrons

Several techniques can be applied to study the properties of the fast electrons that have escaped the target. The traditional choice would be to use a magnetic electron spectrometer [21, 48]. It offers a good energy resolution but the acceptance angle is quite small. Making angular distribution measurements is difficult, especially in a low repetition rate environment. A detector consisting of film and filter layers can be used for the measurement of angular distribution yielding also some information about their spectra, *e.g.* as used by Moore *et al.* (in a wakefield experiment) [49]. This approach is mainly applicable at relatively low energies.

The accuracy of any electron diagnostics placed away from the target is seriously limited due to space-charge effects, which limit the number of electrons escaping the plasma [47]. If all the fast electrons managed to escape, potential on the order of gigavolts could be generated. The space-charge effects thus distort the number of electrons generated, their energy spectrum as well as the angular distribution. For a more accurate characterisation of the fast electrons, in-target electron diagnostics are needed.

In-target electron diagnostics are typically based on generating X-rays within a layered target structure. The X-rays can then leave the target with little loss and

can be detected away from the target by different techniques, *e.g.* PIN-diodes or scintillating detectors. Typically the target structure has layers of selected medium-Z elements that fluoresce at their characteristic K-shell energies as the fast electrons traverse these layers. Electron temperature T can be inferred by comparing the intensity of different lines. Hot-electron temperatures of $200 - 300$ keV have been found at 10^{18} W/cm^2 and the temperature scales approximately as $(I\lambda^2)^{1/3}$ [22, 24].

Fast electrons propagating in matter also lead to emission of bremsstrahlung with a continuous spectrum up to the kinetic energy of electrons. This has been measured by scintillation detectors with different filters and photon energies up to 4 MeV have been observed in Ref. [22]. The increases in laser intensity have resulted in an increase in the electron temperature into MeV range. Such distributions have substantial tails extending beyond 10 MeV. Consequently, there is a need to characterise electrons (and bremsstrahlung) with energies exceeding 10 MeV. Furthermore, it is essential that the detection technique can handle multiple simultaneous hits because of the large number of electrons produced.

Typically X-ray detectors are sensitive to a wide range of energies with a decreasing efficiency towards high energies. Narrow-band energy response up to 100 keV can be created by using different K edge filters. Such filters are easy to construct of thin foils. Above 100 keV the energy selectivity can be achieved by using different thicknesses of high-Z absorber materials like lead (Pb). The thicker the filter the higher the energy where transmission begins. Detectors behind such filters are sensitive to all energies above the 'cut-in' resulting in overlapping energy responses. This makes it necessary to use unfolding techniques to retrieve the incident X-ray spectrum. Such filters work well up to about 1–2 MeV as the X-ray attenuation of lead is decreasing rapidly with energy. However, at about 2 MeV it reaches a shallow minimum and increasing the filter thickness will not shift the cut-in to higher energies anymore. By using an absorber material with a lower-Z the minimum absorption is shifted towards higher energies. Due to the smaller mass-attenuation and lower density the filter thickness quickly becomes impracticable. Energy sensitive detection of bremsstrahlung X-rays above a few MeV's is consequently not feasible by conventional X-ray detectors (like scintillators).

3.3 Photo-nuclear reactions for fast-electron diagnostics

As bremsstrahlung energy reaches about 10 MeV it becomes feasible to apply photo-nuclear reactions for the detection of the energetic photons. In photo-nuclear reactions a nucleus absorbs an energetic photon and the resulting excited state decays through an emission of one or more nucleons, most commonly neutrons. The (γ, n) reactions generally have the largest cross-sections and are easy to detect because the neutrons can escape the target and positron-emitting radioactive nuclides are often produced. The photo-nuclear reactions can thus be detected either by measuring the emitted neutrons or the induced radioactivity in the target structure.

Photonuclear techniques have previously been applied in *e.g.* radiographic X-ray flux monitoring [50]. In high intensity laser-solid research the technique was first introduced in the Petawatt experiments at the Lawrence Livermore National Laboratory (LLNL) [3, 51]. In this thesis the technique has been developed to be applicable in medium-scale (50 TW) experiments at the VULCAN laser [12].

In the photonuclear technique the target is usually a thick slab of high-Z material like lead (Pb) or tantalum (Ta). In such material the kinetic energy of the energetic electrons is efficiently converted into bremsstrahlung. The bremsstrahlung then enters the photo-nuclear activator materials, which become activated. The induced activation is then measured off-line.

3.3.1 Detection by neutrons

The detection of neutrons is probably simplest to implement as any photo-neutron reactions can be detected by this method. However, the neutron detection can be complicated by other possible neutron sources, ion-induced reactions (see Ch. 4) being a particular concern. Neutron detectors are often also somewhat sensitive to γ-rays so the intense bremsstrahlung radiation can blind the neutron detectors. This is a major concern for fast detectors, *i.e.* detectors that can be used for measuring the neutron spectra. Neutron detectors are also bulky compared to the target dimensions so it is not possible to achieve spatial resolution necessary for measuring angular distributions. It is of interest to note that the reactions with the lowest photonuclear reaction thresholds, $^{9}\mathrm{Be}(\gamma, n + 2\alpha)$ and $^{2}\mathrm{H}(\gamma, n)^{1}\mathrm{H}$ with thresholds of 1.7 and 2.2 MeV can only be detected through neutron emission as the reaction products are stable.

3.3.2 Detection by activation

As a neutron is removed from a stable nucleus, the resulting nucleus is often unstable, making it possible to detect the reactions by the induced activation. A few criteria can be set to select reaction candidates. First, the reaction threshold has to be lower than the kinetic energy of the electrons being measured. Second, the decay must produce intense radiation that can be readily detected. Positron emission is particularly suited as coincidence techniques [53] can be applied for background suppression. Third, to allow reasonable time for handling of the samples without excessive counting times the half-life of the reaction product must range from several minutes to an hour. Furthermore, it is beneficial if the parent substance is a readily available in non-hazardous, machinable solid form and the parent nuclide has a large abundance.

Removal of a neutron from a nucleus makes it neutron-deficient and such nuclides decay (if radioactive) nearly always either by positron emission or by electron capture. Positron emission is more common for light elements but it is rare for heavy elements, except if several neutrons are removed. In heavy elements, the decay energy is often not large enough to make positron decay energetically possible.

The positron-emitting nuclides are easy to detect as the positrons quickly annihilate with electrons producing two 511 keV photons flying into the opposite directions. These can be detected by simple NaI(Tl) scintillation detectors placed on both sides of a source. Typically, background events occur at random intervals in each detector, so counting only events that occur in two detectors nearly simultaneously (in coincidence) results in efficient suppression of the background.

The electron capture decays are considerably more difficult to observe. If the nuclide emits nuclear γ-rays they can be measured by a high-resolution germanium detector. In many cases, there are no strong nuclear γ-rays. Then the only way to

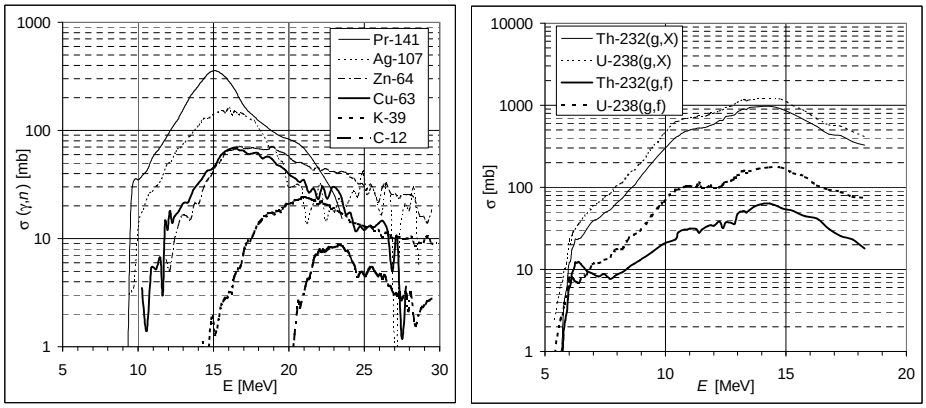

FIGURE 3.1. *Reaction cross-sections for* (γ, n) *reactions studied in this work (left). Cross-sections for all photon-induced reactions* (γ, X) *and photo-fission reactions* (γ, f) *of uranium and thorium (right). Plotted according to data from the* EXFOR *database [52].*

detect the decays is by characteristic X-rays. Such measurements can be greatly complicated by self-absorption in the activated sample. The background is of greater concern for gamma spectroscopy than for coincidence measurements as there is no way to discriminate background events. For these reasons, the initial studies concentrated on the positron emitting nuclides.

The cross-sections for the photo-nuclear reactions used in this study are shown in Figure 3.1. As a rule of thumb, the photo-neutron reaction threshold decreases and the peak cross-section increases with mass number. Typically, the threshold is about 20 MeV for the light elements (like carbon), close to 10 MeV for the medium-heavy elements (like copper) decreasing to about 5 MeV for the heaviest nuclides like thorium and uranium. Typical peak cross sections are 10 mb, 70 mb, and 1000 mb, respectively. The decrease in reaction threshold is a consequence of the decrease in neutron binding energy in heavier elements. The cross-section usually peaks somewhat above the reaction threshold due to the giant dipole resonance, which results from large collective oscillations of the nucleus. The shape of the resonance for numerous nuclides has been extensively studied as valuable information about the nuclear structure can be inferred from it [54].

The principal photo-nuclear reaction used in this thesis is ^{63}Cu$(\gamma, n)^{62}$Cu. This was chosen due to several reasons: ^{62}Cu is an essentially pure positron emitter with 9.7 min half-life, the reaction has a modest threshold and large cross-section. Furthermore, ^{63}Cu is abundant isotope in natural copper (about 69 %) and copper is a common engineering material. It is easily available in very pure forms and it is chemically nearly inert under typical room conditions. Other reactions studied are described in more detail in Table 3.1 on Page 20.

3.3.3 Photofission

The (γ, n) reaction is the simplest photo-nuclear reaction. More complicated reactions like the emission of several neutrons also exist, in particular, with higher photon

energy or for heavy nuclei. A particularly interesting reaction is the photo-fission of heavy elements like thorium and uranium. Even though fission is energetically always possible a sufficient excitation of the nucleus must be established before it is torn apart by electrical repulsion forces. In neutron-induced fission this energy is mainly supplied by the binding energy of the incident neutron. In photo-fission, it is supplied by the incident photon. The fission cross-sections for ^{232}Th and ^{238}U are shown in Figure 3.1 along with the total photon-induced cross-sections.

Fissions can be detected by three means: neutrons, fission fragments and the characteristic γ-rays of the fission products. Detection of fission neutrons suffers from the same ambiguity as the photo-neutron reactions — there are many potential sources of neutrons. However, in addition to producing *prompt* neutrons at the moment of fission, some *delayed* neutrons are produced in the decay of highly-unstable fission products. Because these neutrons can be emitted up to minutes after the fission, detecting them would serve as a unambiguous proof of fission. Detecting fission fragments by *e.g.* particle track detectors could also be used for detection. Their range, however, is so short that only if the fission occurred close to surface would they be able to reach the detector.

The method employed in the present studies is the γ-ray spectroscopy of the fission products, even though it is complicated by the strong background radioactivity of the natural samples. The fission products have a wide spectrum of half-lives, so the activity measurements can be carried out on several time-scales. Detecting the characteristic γ-ray energies of several fission products in combination with correct half-life serves as the proof of fissions in the experiment.

Fission can also be induced directly by fast electrons. This process is predicted to be significant in the focal spot if laser is irradiating the fissioning material directly [55] and could result in an extreme flux of fission fragments. This process has a very small cross-section ($\approx$ 1 mb [55]) but the effective electron fluence in the focal region can be very large due to the large number of oscillating electrons. Outside the focal region, bremsstrahlung-induced photo-fission is estimated to dominate as the electron fluence is much less. In the present experiments, the direct laser-irradiation of uranium was not attempted, and hence, the results are believed to be due to photo-fission.

Even after establishing the occurrence of fission reactions in the experiments, there remains some doubt about the precise mechanism. In principle, the fissions could be induced by neutrons emitted in photo-neutron and ion-induced reactions. However, the neutron fluxes are much lower than the energetic photon fluxes while there is only about an order-of-magnitude enhancement in the cross-sections. Consequently, the most likely mechanism is photo-fission [56].

3.4 Generation of bremsstrahlung in the radiation converter

Electrons produced in the laser-plasma interaction are slowed down in the radiation converter material. This is a stochastic process where multiple collisions with ions and electrons result in a part of the kinetic energy being transformed into bremsstrahlung X-rays and the rest to the background electrons (*i.e.* heat). Bremsstrahlung is emitted in a continuous spectrum up to the instantaneous kinetic energy of the electron, into a cone with half-angle approximately $1/\gamma$ [57]. The brems-

strahlung theory applies well to the low (< 2 MeV) and high (> 50 MeV) energies, and the intermediate energies are treated by interpolation techniques [58].

Ions are more efficient than electrons in deflecting electrons due to their bigger charge, hence there is a $1/Z^2$ dependence in the bremsstrahlung cross-section. To maximise the bremsstrahlung yield it is advantageous to use a high-Z material (like lead or tantalum) as the radiation converter material. In tantalum, the critical energy where the loss through bremsstrahlung equals the loss through collisions is about 7 MeV and the radiation length (describing the energy loss to bremsstrahlung per distance) is 4.2 mm [59]. The total radiation yield (in Ta) is about 30% at 10 MeV and increases to 50 % at 30 MeV [60].

To determine the total bremsstrahlung spectrum, the electron slowing down in the converter material must be taken in account. Electrons are also gradually deflected away from their original trajectory due to the multiple small-angle collisions. This leads to a wider emission cone than the instantaneous $1/\gamma$. To understand better the spectral and angular properties of bremsstrahlung generated under the conditions of this work, a number simulations were carried out by Monte-Carlo particle code GEANT [61].

In the GEANT simulations, the electrons are incident on a 3 mm thick Pb slab at a variable angle of incidence, spread into a cone with a variable cone angle. The electrons can be either monoenergetic or they can be taken from a Maxwellian ($f(E) = f_0 \exp(-E/kT)$) or a relativistic ($f(E) = f_0 E^2 \exp(-E/kT)$) spectrum. Large magnetic fields inside solid targets are predicted in computer simulations. To study the effect of these a magnetic field profile could optionally be defined and switched on inside the target.

A few bremsstrahlung spectra resulting from monoenergetic electrons are shown in Figure 3.2. Starting from the incident energy E_0, a sharp cut-on at 2–3 MeV below E_0 is observed. Below this the photon spectrum is relatively flat increasing slowly from 0.01 to 0.1 photons per MeV per incident electron. The photon yield is only weakly sensitive on the initial electron energy at energies much below the initial.

The fact that even a monoenergetic electron spectrum results in the emission of a wide spectrum of bremsstrahlung complicates the application of the photo-nuclear technique for measuring the electron spectrum. Use of unfolding techniques is generally necessary or the spectrum can be assumed to follow a functional form, *e.g.* exponential, and the function parameters can be optimised for best fit to data.

3.4.1 Angular distribution

In the simulations it was observed that the bremsstrahlung spectrum is the hottest in the direction of the initial electron propagation and a substantially cooler spectrum is observed in oblique directions. This is illustrated in Figure 3.2 where spectra measured at angles 0 to 20 degrees and 45 to 60 degrees from the incident direction are shown.

This results from the fact that 'instantaneous' bremsstrahlung of is directed in a narrow cone along the direction of propagation of the electron. Forward-directed bremsstrahlung is thus mainly generated by electrons that have not yet deviated from their initial direction or lost much energy. In multiple collisions, electrons gradually lose kinetic energy and are deflected from their original direction. Such

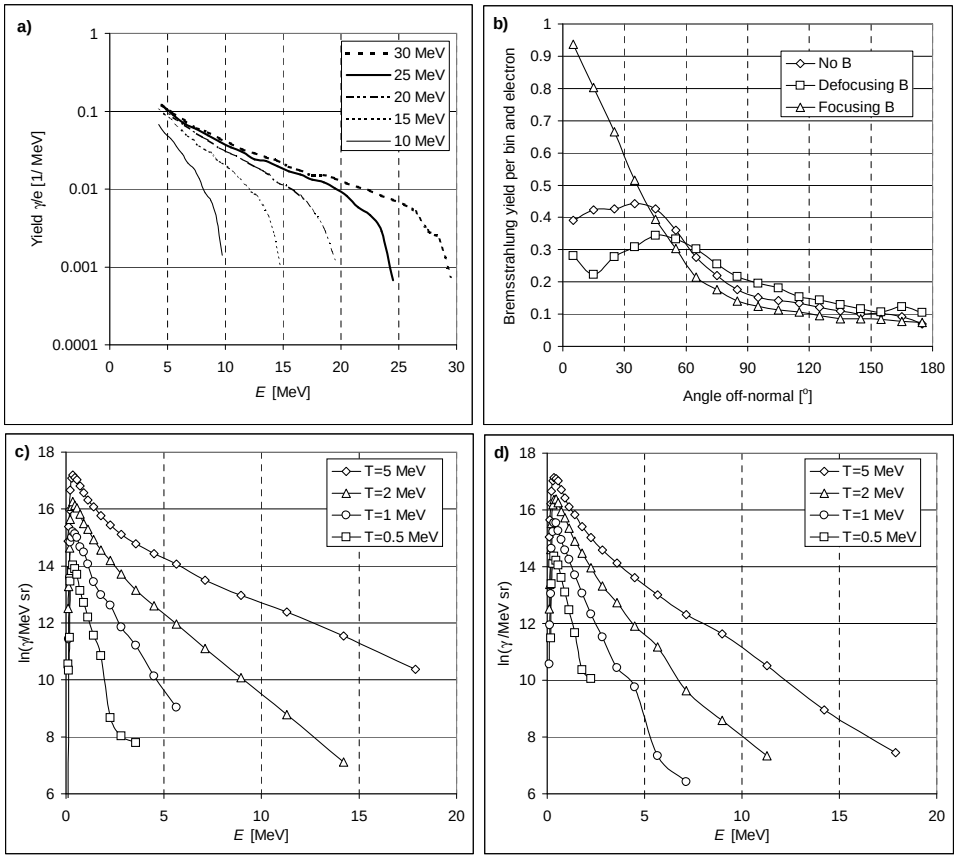

FIGURE 3.2. *Selected results from the* GEANT *simulations carried out in this work (unpublished). (a) Absolute bremsstrahlung spectral yields with monoenergetic electrons. (b) The effect of magnetic field on the angular distribution of electrons. An electron jet with 30° angular divergence is incident on target surface at 45° off-normal. The resulting angular distributions with no internal magnetic field and with a focusing and defocusing magnetic field are presented. (c) and (d): The bremsstrahlung spectrum with different exponential electron spectra normally incident on target as determined (c) 0°—20° off-normal angles and (d) 45°—60° off-normal angles.*

electrons generate the oblique bremsstrahlung. Consequently, the oblique spectrum is softer than the forward-directed.

3.4.2 Effect of magnetic field

Very large electron currents are generated in the laser-plasma interactions. If 25 J of energy was absorbed and converted into 1 MeV electrons in 1 ps time, a current of 25 MA would be generated. Even though it will be largely neutralised by return current, the generation of large magnetic fields is highly plausible. In simulations, magnetic fields of several hundred Teslas have been observed in bulk material due to these electrons [62] and up to 10000 T in the laser-plasma interaction region [31]. The bulk fields are observed to collimate the incident electron beam into a narrow channel, despite a relatively large spread of incidence angles. Such collimation could conceivably affect the angular distribution of bremsstrahlung.

The effect of the bulk magnetic field on the propagation of the electrons and the angular distribution of bremsstrahlung was also studied by predefining a magnetic field structure in the bulk. The electrons were incident in a cone on the target surface and the results were compared to the unmagnetised case (see Fig. 3.2). Collimation in the emitted bremsstrahlung is clearly observed. However, in the case of unidirectional electron beam along the target normal, little effect is seen. This is an indication that the multiple small angle scattering does not deflect the electrons significantly before the emission of the energetic bremsstrahlung. However, if electrons are incident on target in a substantial angle, they may be collimated along the magnetic field axis.

3.5 Experimental results

Initially a crude proof-of-principle experiment was carried out to demonstrate the feasibility of photo-nuclear activation in an experiment at moderate laser powers achievable at the Vulcan laser. In the second phase a more detailed study with two main goals, measurement of angular distributions and study of different reactions including photo-fission, was conducted. The initial experiment is detailed in Ref. [Publ1], and the further studies of angular distributions and different nuclear reactions in Refs. [Publ2] and [Publ3].

3.5.1 Initial experiments

In the initial experiment the laser beam was focused by f = 1 on-axis parabola on the target surface at 45° angle from target normal. Some small copper pieces were attached to the target mount in a way that minimised the beam obstruction. Due to radiation exposure concerns the target/converter Z was increased only gradually. Initially BK-7 glass (essentially SiO_2) and aluminium were used but with no success. As well, copper alone proved unsuccessful. Finally, the laser was fired directly on a 3 mm thick lead slab backed by 3 mm of copper. Substantial activation of copper with decay time matching the half-life of ^{62}Cu was observed by coincidence counting of the positron annihilation radiation.

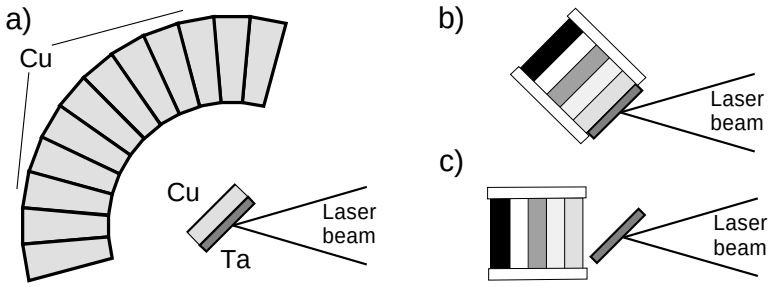

FIGURE 3.3. *Schematic drawing of the angular distribution target (a) and two examples of the multi-element set-up: for a small scale-length (b) and for a large scale-length (c).*

A crude angular distribution measurement was also carried out by placing several small copper pieces around the main target. A narrow γ-ray beam close to the target normal was observed as detailed in Ref. [Publ1]. This would suggest that the fast electrons were generated by *e.g.* Brunel-like mechanism that accelerates electrons in the direction of the target normal, at an angle close to 45° from the direction of laser propagation.

It should be noted that in this experiment the Vulcan laser was operating with an exceptionally small pre-pulse resulting in little pre-plasma formation and a small plasma scale-length during the main pulse. This was determined from shadowgraphic probe images taken just before the main pulse.

3.5.2 Study of angular distributions

To study the angular distribution of the electrons in more detail a special target was designed (see Fig. 3.3a) based on the results from the early experiment. The radiation converter material was changed from lead to tantalum to minimise harmful contamination in the experimental chamber but still maintaining a high Z. The thickness of tantalum (1.75 mm) was chosen to have a mass density close to the lead slabs used in the initial experiment. The tantalum slab was backed by a 3 mm thick slab of copper, which acted as an overall activation reference. Twelve wedged copper segments surrounded the target, each spanning a 10° sector. The directions covered were up to 60 degrees from target normal on both sides.

After each shot the angular distribution of activation was obtained by measuring the activity in each copper segment and correcting for decay. A few examples of the measured distributions are shown in Fig. 3.4. They are proportional to the distribution of the fast electrons if their spectrum is not angle-dependent. If the spectrum is direction-dependent the activity distribution reveals the angular distribution of the most energetic electrons as the activation probability is sensitive to the electron energy.

The size of the pre-plasma was measured by a shadowgraphic technique [34] like in the early experiment. A typical recorded shadowgraphic image is shown in Figure 3.5. The size of the pre-plasma could be varied by changing the duration of a low-power pedestal preceding the main pulse (accomplished by varying Pockel cell timings in the laser chain) or by introducing deliberate prepulses. By changing the

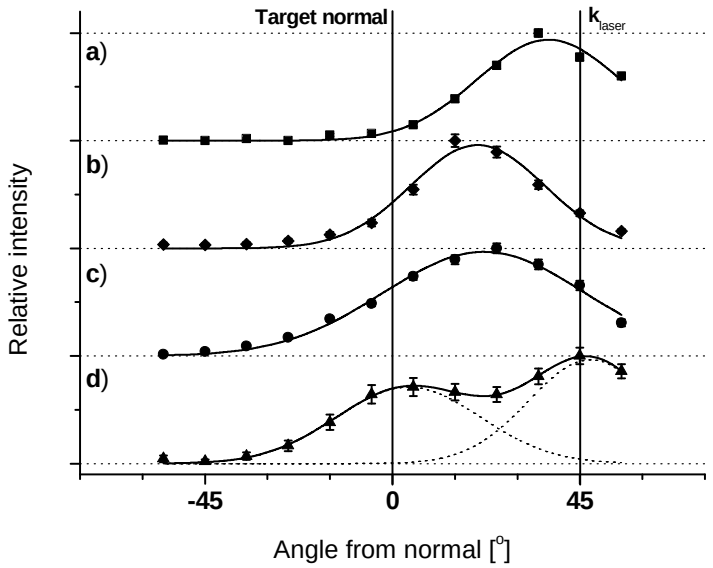

FIGURE 3.4. *Selected angular distributions of bremsstrahlung, scaled and offset for clarity: a) large scale-length, b) small scale-length, presence of different mechanisms demonstrated by c) a very wide distribution and d) double-peaked structure. The lines indicate the best-fit Gaussian distributions (sum of two Gaussians in d)). [Publ2]*

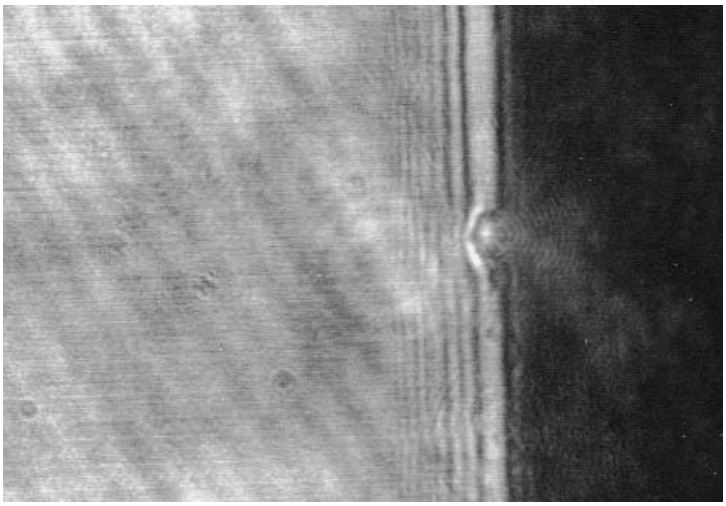

FIGURE 3.5. *A sample shadowgraphy image imaged by probe laser before the main laser pulse. The pre-plasma is clearly visible. (unpublished)*

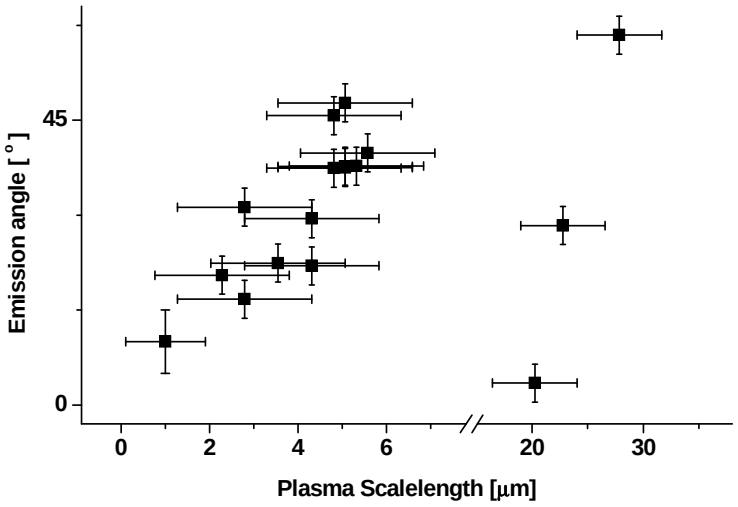

FIGURE 3.6. *The measured direction of main brensstrahlung emission as the function of the size of preplasma. [Publ2]*

size of the preplasma one is able to control the plasma scale-length at the time of the main laser-plasma interaction.

In this experiment, the main γ-ray beam was usually directed at the angles between the direction of laser propagation and the target normal. A correlation between the plasma scale-length and the direction of energetic γ-rays was found, as shown in Figure 3.6. At very large plasma scale-length, an uncorrelated behaviour was observed.

The observed behaviour of the direction vs. scale-length can be explained by a change in the dominating absorption mechanism at different scale-length. Brunel-like or resonance absorption mechanisms dominate at small scale-lengths, generating fast electrons predominantly in the direction close to the target normal. As the scale-length is increased, the ponderomotive $\mathbf{v} \times \mathbf{B}$ mechanism generating electrons in the direction of the laser beam starts to dominate. At intermediate scale-lengths, two separate beams were occasionally observed suggesting that two different mechanisms act simultaneously. The uncorrelated behaviour at very large scale-length is likely to result from laser and electron beam propagation instabilities (like self-focusing and hosing) in the large underdense plasma.

3.5.3 Study of different reactions

Activation by several different, simultaneous nuclear reactions can be applied to measure the spectrum of the fast electrons. Demonstrating that certain reactions can actually be induced serves also as a reference for potential practical applications. For these purposes, a different target was designed that allowed simultaneous irradiation of several different materials by the bremsstrahlung beam generated in the tantalum converter (see Fig. 3.3). A variation of this design was used to demonstrate photo-fission in laser-plasma experiments. In this part of the work there was

TABLE 3.1. *Photo-neutron reactions studied by positron emission. Principal reaction parameters and the half-life of the reaction products are also shown [52, 63].*

Target	x_n [%]	Q [MeV]	$\sigma_{\max}$ [mb]	$T_{1/2}$ [min]
^{63}Cu	69.2	10.9	69	9.7
^{12}C	98.9	18.7	9	20.4
^{35}Cl	75.8	12.7	25	32.0
^{39}K	93.3	13.1	24	7.6
^{65}Zn	48.6	11.9	72	38.5
^{107}Ag	51.8	9.6	160	24.0
^{141}Pr	100	9.4	360	3.4
^{232}Th	100	6.4	970	
^{238}U	99.3	6.2	1220	

intense collaboration with the group from the Glasgow University.

The studied activation materials are shown in Table 3.1. Copper (Cu) was the principal activation material. Other elements were praseodymium (Pr), element with lowest threshold for production of a β^+ active reaction product and a large cross section. Silver (Ag) has a lower threshold than copper but the activation product has an isomeric state with a long half half-life (8 days), and its contribution to the tabulated (γ, n) cross-section is unknown. Zinc (Zn) has a cross-section similar to copper but slightly more peaked. Potassium (K) and chlorine (Cl) have higher reaction thresholds and cross-sections peaking above 20 MeV. They were studied simultaneously in the form of potassium chloride (KCl), and reaction products were identified through the different half-lives. Finally carbon (C) was used as the element of highest threshold (nearly 20 MeV).

In addition to the isotopes detectable through their positron emission, the tantalum converters were measured by high-resolution Ge detector to detect characteristic X-rays and low-energy γ-rays from reaction ^{181}Ta$(\gamma, n)^{180}$Ta. It is the only way to detect the ^{180}Ta decays. Gamma spectroscopy was also applied for the detection of photo-fission.

The activation samples were 2-3 mm thick elemental slabs (except KCl) that were stacked behind the converter. The total thickness of the stack was up to 15 mm. In the experiment, the direction of the γ-ray beam was found to vary on shot-to-shot basis so much that not all the activation samples were equally irradiated. This greatly complicated the spectral analysis. The demonstration of multiple simultaneous reactions was more successful, and all the intended reactions (except Cl in KCl) were observed. The produced isotopes were verified by measuring their half-lives. Some of the measured decay curves are shown in Figure 3.7. The counting statistics for K and C were poor, and the lack of Cl signal can be explained by the longer half-life of ^{34m}Cl compared to ^{38}K. In copper, the 12.7 h half-life of ^{64}Cu was observed in addition to ^{62}Cu. This was expected as ^{64}Cu is produced from the other abundant copper isotope, ^{65}Cu.

The activity in the copper slab behind the tantalum radiator showed large shot-to-shot variations. The initial activity ranged from 6 to 2200 Bq. The average was 460 Bq, standard deviation 510 Bq and median 300 Bq. Below 10^{18} W/cm^2 there was little activation but otherwise there was no correlation with intensity. No correlation

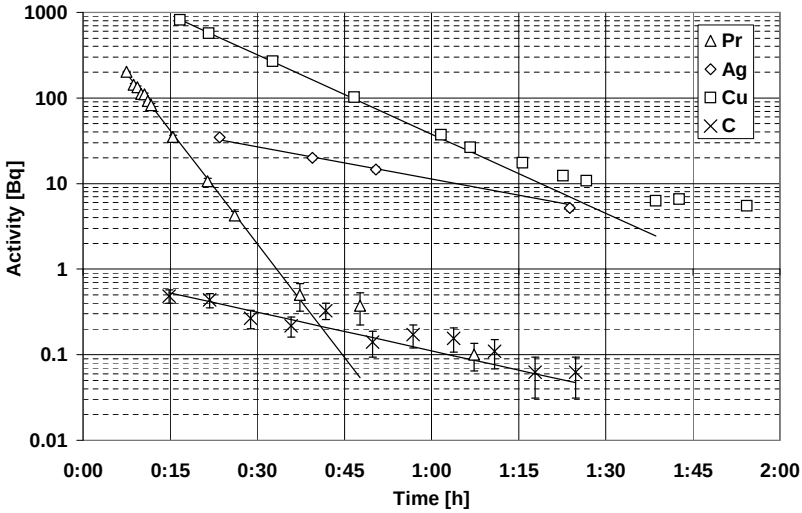

FIGURE 3.7. *The observed decay of several materials. Lines indicate the best-fit to data (with the half-lives from Table 3.1). The copper data shows a contribution from the decay of* ^{65}Cu*. Error bars indicate the* 1σ *uncertainty of the measured activity.*

with plasma scale-length was observed suggesting that the different mechanisms have similar efficiency of fast electron production. The lack of correlations can be explained by the fact that only a tail of the total electron distributions is energetic enough to exceed the photo-nuclear reaction threshold. Other measurements indicate that the electron temperature is about 1–2 MeV. Hence, a small variation in temperature can cause a large change in the number of electrons above thresholds, and such variations can mask correlations.

For the fission measurement, the multi-element stack was replaced by a sealed aluminium capsule containing a $10 \times 10 \times 2$ mm slab of uranium or thorium. A tantalum slab was still used as laser target, in order to achieve efficient bremsstrahlung generation while avoiding direct exposure of the aluminium capsule to laser light. The capsule was irradiated for three laser shots, replacing the tantalum converter after each shot. After irradiation, it was taken to a germanium detector for high-resolution spectroscopy. The γ-ray spectrum was compared to a background spectrum measured before irradiation. In the case of uranium, the spectra measured after irradiation showed clearly numerous lines, and these were shown to match that of several fission products as detailed in Ref. [Publ3]. In thorium, the higher natural background masked the fission product lines.

CHAPTER 4

Ions in laser-solid experiments

In several laser-solid experiments, jets of large numbers of energetic protons and heavier ions have been observed. Energetic protons with energies up to 58 MeV [35, 64, 65, 66, 67, 68, 69] and heavy ions with much higher energy have been observed [35]. The number of accelerated ions can be large: with VULCAN, up to 10^{12} protons above 2 MeV have been reported [65]. This corresponds to about 1 J of energy, in a laser shot with laser energy of 50 J. In Petawatt experiments, 3×10^{13} protons above 10 MeV, corresponding to 48 J (12% of laser energy) have been observed [69].

The fast ions can be interesting for several practical applications. In principle, laser plasma could act as a compact particle accelerator producing dense, temporally short ion bunches. Some examples for uses for such beams are probing dense plasmas, treating material surfaces and production of neutron-poor radionuclides, a replacement for cyclotrons. Medical uses, either direct like radiation therapy or indirect (like use of the radionuclides) can be envisaged as well.

4.1 Ion acceleration

The precise mechanisms producing the energetic ions are still open to scientific debate. Even conflicting data regarding the origin of ions has been recently published (see *e.g.* Refs. [25, 35, 65, 69]). Several mechanisms can be seen to contribute to the fast ion production, but their relative importance cannot yet be stated with certainty. Generally, ion motion is believed to be a secondary effect after electrons are first set in motion. The charge-separation fields then lead the ions in motion, unless a neutralising return current is present. Often ions can be treated immobile during the laser pulse, however, at the highest intensities, their motion may become significant.

The simplest ion acceleration mechanism is the ambipolar diffusion in plasma expansion, acting mainly after the laser pulse. The hot plasma created in the laser-plasma interaction starts to expand. Initially, the electrons are hot ($T_e \approx 1$ MeV) and moving fast. The electrons are prevented from leaving the plasma by the build-up of space-charge fields. The ions are accelerated in this field allowing the plasma to gradually expand. A part of electron kinetic energy is transferred to the ions. Plasma expansion results in a relatively wide and uniform spatial distribution of the ions. The picture is possibly complicated by self-generated magnetic fields due to non-parallel density and temperature gradients fields. Typically, the ions have a nearly exponential energy spectrum and their energies extend to a few MeV [65].

The plasma expansion alone is not sufficient to explain all the fast ions generated in laser-plasma experiments. It mainly explains a part of the ions observed in the plasma blow-off. A variation of this mechanism presented by Hatchett *et al.* [25] predicts a formation of a thin electrostatic sheath layer at the rear surface of the target by fast electrons that have traversed the target. Because the number of electrons is extremely large and there is no pre-plasma at the rear surface the layer is very thin and resulting electric field very large ($\approx 10^{12}$ V/m). This field would accelerate

the ions at the rear surface of the target and could explain the large number of ions observed behind the target in the Petawatt experiments.

Ions can also be accelerated at the critical surface during the laser pulse. The ponderomotive force acting predominantly on electrons can produce large fields. At 10^{19} W/cm$^2\mu$m^2 the ponderomotive potential is about 1 MeV. This potential difference occurs approximately over the plasma skin-depth (c/ω_p). Plasma waves driven at the critical surface may also produce large fields. Within the target material, ions can be accelerated further by fields induced by intense fast electron currents [65] and their trajectories can be affected by magnetic fields [35]. Phenomena at the critical surface can be seen to accelerate ions into the target as well as into the blow-off direction.

4.2 Conventional ion detection

Ions can be detected by various conventional detection techniques like plastic track detectors (CR-39) and film-based detectors. Generally, the detection is based on the intense ionisation and subsequent bulk damage caused by ions in solid matter. Ions are stopped at much shorter range than *e.g.* electrons of same energy. This allows for discrimination between X-rays, electrons and ions.

The benefit of the plastic track detectors is that they are only sensitive to ions. Each ion (above threshold of about 200 keV) leaves a bulk damage track in the plastic material. The microscopic damage can be made visible in an etching process. Individual ion tracks can then be counted under microscope. Track detectors are capable of detecting single ions, however, at high fluence the counting can become tedious or the detector may saturate. Different ion species can be separated as heavy ions leave thicker tracks due to more rapid energy deposition.

Film detectors are sensitive to the electrons created by the stopping ions. Consequently, they are also sensitive to background X-rays and electrons. Typically, in film detectors the change in optical density is proportional to the absorbed dose. In principle, semiconductor detectors can also be used but the cumulative ion dose may have adverse effects on their semiconducting properties.

Ion detectors used alone are not very practical as they provide little information on the ion spectra and number of ions. A small pinhole can be placed between the laser-plasma and an ion detector to obtain a pinhole image of the ion source. This technique with CR-39 detectors has been applied in imaging ions from laser-plasma interactions [64, 70].

To obtain spectral information spectrometer techniques can be applied. In the simplest case, the ion blow-off is obstructed by a pinhole and transmitted ions are then deflected by magnetic field. The ion deflection is inversely proportional to the ion momentum. Hence, ions of different energies hit different spots on the detector material behind the bending magnet.

A simple magnetic spectrometer has the drawback that it does not distinguish different ion species, as deflection is dependent on charge-to-momentum ratio. This can be improved by the use of a Thompson parabola, a device where the deflection field is a combination of parallel magnetic and electric fields. The additional deflection by the electric field is dependent on ion energy resulting in complete separation of ions

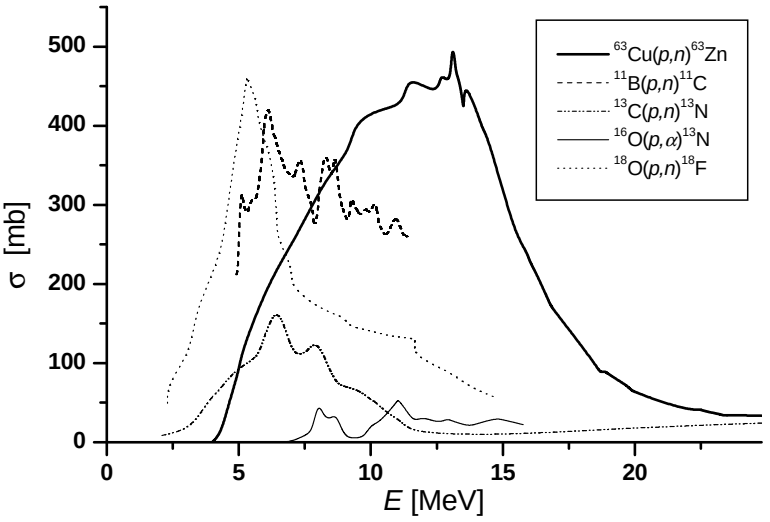

FIGURE 4.1. *Reaction cross-sections for selected proton-induced reactions.* EXFOR *[52].*

with different charge-to-mass ratios. The deflection pattern is a parabola. Simple static fields cannot separate ions with equal charge-to-mass ratios.

4.3 Ion-induced nuclear reactions as a diagnostic

Protons with more than a few MeV of kinetic energy can induce nuclear reactions in most materials. The simplest reaction in most cases is the (p, n) reaction. This reaction can have a low threshold energy as the number of nucleons in the nucleus does not change, and hence the binding energy of a nucleon need not be supplied. This is in contrast to the (γ, n) reactions where a neutron is removed from the nucleus and the photon must be able to supply its binding energy. On the other hand, the incident proton must be sufficiently energetic to overcome the Coulomb barrier of the nucleus. This leads to diminishing cross-sections and increasing reaction thresholds for the heavy elements.

The nuclides produced through the (p, n) reactions are generally neutron-deficient, and hence they decay either through positron emission or electron capture. Many of the reactions with low thresholds produce nuclides with relatively long half-lives and decay by electron capture. For diagnostic purposes it would be advantageous to use reaction products which decay through positron emission and have a half-life of tens of minutes, for the same reasons as such nuclides are desirable for the (γ, n) reactions. Such nuclides can be produced by numerous reactions with thresholds of about 5 MeV. The most commonly used reaction in this thesis was the ^{63}Cu$(p, n)^{63}$Zn reaction in natural copper. ^{63}Zn decays mainly (92.7 %) by β^+ decay with a 38.47 minute half-life and it does not have strong interfering nuclear γ-ray in coincidence with positron emission, making it a nearly ideal diagnostic.

The peak cross-sections for the (p, n) reactions are generally an order of magnitude larger than for (γ, n) reactions for relatively light elements. Some examples of

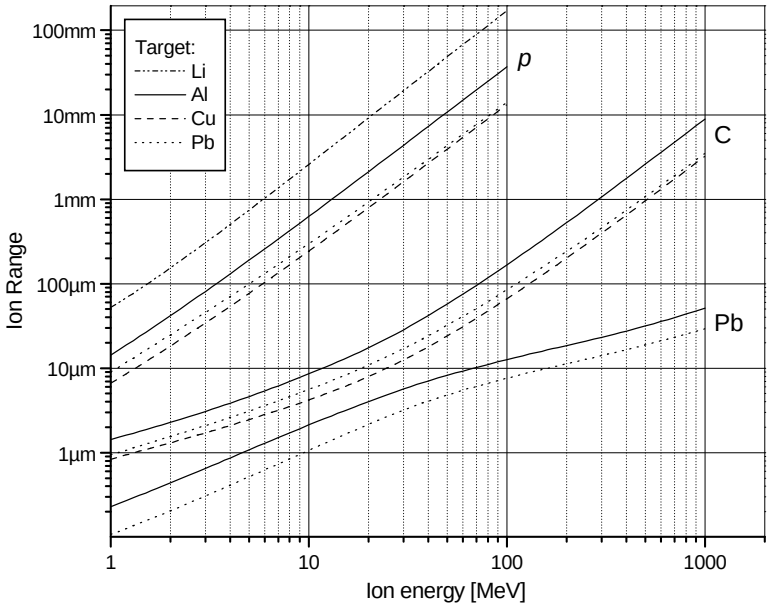

FIGURE 4.2. *Range of protons, carbon and lead ions in selected metals as calculated by* SRIM *[71]. The line style indicates the target material and the labels show the ion type.*

the cross-sections are shown in Figure 4.1. Comparing these to Figure 3.1 the much larger cross-sections and lower thresholds are evident. On the other hand, the protons are stopped much faster in solids than γ-rays. As an example, the ranges of 10 MeV and 20 MeV protons in copper are 0.25 and 0.8 mm while γ-rays at the same energies have mean free path of 36 and 33 mm, respectively. Hence, compared to bremsstrahlung ions can be detected by relatively thin detectors.

4.3.1 Spectral diagnostic

The energy loss mechanism is very different for protons compared to γ-rays. Protons lose their energy in a nearly continuous manner in many small-angle collisions with electrons at a very predictable rate [72]. γ-rays are attenuated in only a few distinct events instead. Therefore, for ions it is possible to calculate the remaining kinetic energy accurately after a given distance in solid but not for γ-rays. Some typical ion ranges are shown in Figure 4.2.

A diagnostic for measuring the spectrum of ions can be constructed using a single element and a single nuclear reaction by making use of the continuous slowing-down. By stacking several thin foils each foil is exposed to ion spectrum that has been slowed-down by the preceding foils. Consequently, each foil is sensitive to successively higher incident ion energies and the incident spectrum can be unfolded from the induced activity in each foil.

In this work, ions were measured by Cu foil stacks consisting of several foils with increasing thickness: a stack with five 20 μm, three 100 μm and one 250 μm foil was

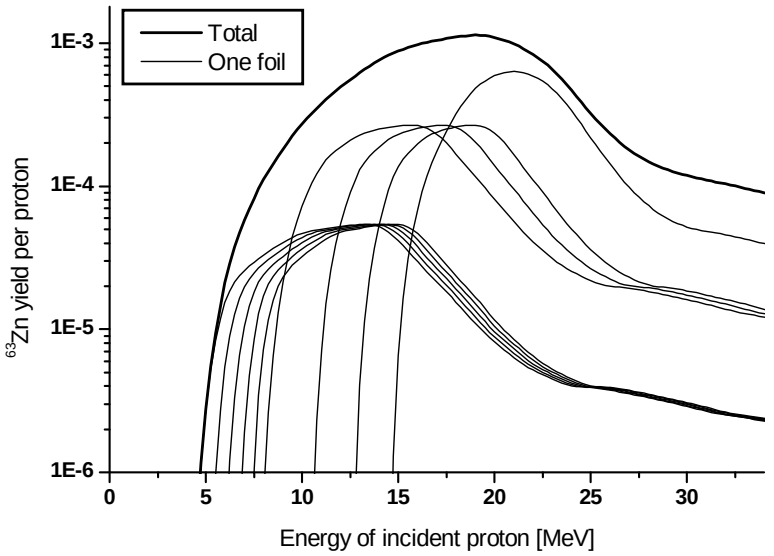

FIGURE 4.3. *The activation response of a typical activation foil stack (thin lines) with foil thickness [μm] from top: 5×20, 3×100, and 250. The thick line indicates the total response of the stack.*

typical. The response of each foil in such a stack is shown in Figure 4.3. Typically, there are much more low-energy protons than high-energy ones, and such stack provides high resolution at low energies and less resolution at high energies where the activation signal is weaker. The proton spectrum can be found by unfolding from the activity of the individual copper foils.

The sensitivity of the Cu activation detector can be estimated assuming all the foils were counted together. The ^{63}Zn yield in the entire stack is also displayed in Figure 4.3. Only slightly above the threshold production rate exceeds 10^{-4} per proton and reaches a maximum of 10^{-3} per proton at 20 MeV. The maximum is caused by the finite thickness of the stack used. In a typical 100 s counting period, about 300 ^{63}Zn nuclei produce one count, so about 10^6 protons at 10 MeV (as an example) are needed for one count. The detection threshold is thus a few million protons.

The total kinetic energy carried by the ions can also be calculated from the measured activation. With 10 MeV protons, the production rate of ^{63}Zn is about 1.7×10^7 nuclei per Joule of energy in the ions corresponding to an activity of 50 kBq. This rate is fairly sensitive to the ion energy: 7 MeV protons would yield 11 kBq/J and 15 MeV protons 170 kBq/J.

Compared to ion spectrometers the ion activation diagnostic can detect ions over a large solid angle. Hence, the total ion production is easy to measure. The results are likely to reflect the 'overall' properties of the emitted ions. However, due to the wide energy response of different foils its capability to resolve spectral details is limited. It is well suited for large ion fluxes but at low fluxes the poor counting statistics limit its accuracy. The activation diagnostic is completely insensitive to other particles, to lower-energy processes and to electrical noise generated by the laser-plasma interaction. It shares many of the advantages of the CR-39 detectors

but is better for large ion fluxes.

4.3.2 Heavy ion reactions

The plasma blow-off has been found to contain also large quantities of very energetic heavy ions in addition to the protons. Fully ionised carbon ions up to 60 MeV and lead ions up to 400 MeV have been detected in the plasma blow-off [67]. Especially the carbon ions appear to be energetic enough to induce nuclear reactions [73, 74].

Characteristic to the heavy-ion induced nuclear reactions is a great variety of possible reaction products. Not only is complete fusion of the colliding nuclei possible ([74]) but a varying number of nucleons can be evaporated from the compound nucleus. Cross-sections for producing various end-products by light ions in aluminium have been measured in [73]. The reactions producing ^{34m}Cl (^{27}Al(^{12}C, αn)^{34m}Cl and ^{27}Al(^{12}C, $3n2p$)^{34m}Cl), are the easiest to realise with cross-section extending to below 20 MeV. The cross-section peaks at 20–50 MeV and has a value of 60–75 mb in this range. ^{34m}Cl further more has a convenient half-life of 32 min and several strong γ-rays (146, 1176, 2127, and 3304 keV) making it an easy candidate for the detection of heavy-ion reactions. The complete fusion reaction would have a cross-section of about 1000 mb but only above 40 MeV [74] and the reaction product ^{39}K is stable.

Even though the kinetic energy of the heavy ions appears to be large, their range in solid matter is only a fraction of that of protons (Fig. 4.2). Only about 20 μm of aluminium is needed to slow 40 MeV carbon ions to 20 MeV. Hence, thin foil targets are optimal for detection of heavy ion reactions. By stacking several thin foils, some spectral information could be obtained. Stacking can also be used to confirm that the activation is induced by heavy ions and not by anything else. Because of their short range, the heavy ions induce activation only close to front surface while all other particles would induce activation in a much larger volume.

4.4 Experimental results

The activation experiments were conducted in several phases. Initially only single thick foil (250 μm) activators were exposed to plasma blow-off. This was to show the feasibility of producing ion-induced activation, to identify the produced nuclides and to get estimates of total activation yield. In this phase several activation reactions were also demonstrated [Publ4]. After this, spectral studies using thin foil stacks were conducted initially for the blow-off plasma and later simultaneously on both sides of the target. Finally, heavy ion reactions were studied by adding thin aluminium foils to the copper spectral stacks.

4.4.1 Activation in different materials

From the very beginning it was obvious that ion activation had some potential as an ion diagnostic: a 250 μm thick copper foil placed about 0.5 m away from target and mostly shielded by other diagnostics was found to be slightly activated. Consistently activities of about 1 kBq were obtained with similar foils but spanning 0.02 sr and directly exposed to plasma blow-off.

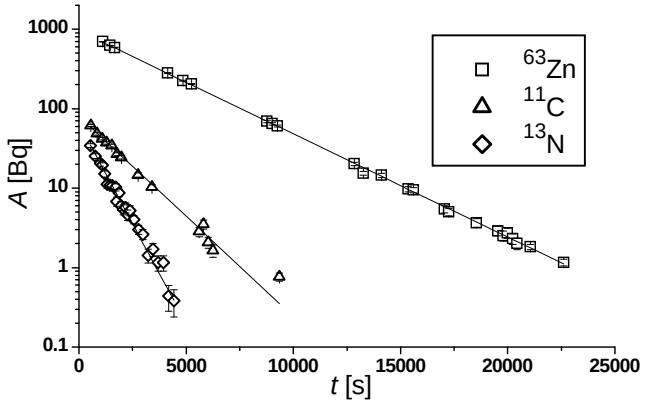

FIGURE 4.4. *Selected decay curves measured by positron coincidence counting. The half-lives correspond to ^{63}Zn in copper, ^{11}C in Pyrex and ^{13}N in plastic.*

Exposing different materials to plasma blow-off several other activation reactions were observed [Publ4]. These were identified by half-life monitoring as shown in Figure 4.4. The half-life of activity in copper was found to correspond to ^{63}Zn as expected. In Pyrex, ^{11}C with 20 minute half-life was observed. This can be produced from boron by $^{11}\mathrm{B}(p,n)^{11}\mathrm{C}$ reaction. In plastic foil, production of ^{13}N with 10 minute half-life was demonstrated. ^{13}N can be produced either from oxygen by $^{16}\mathrm{O}(p,\alpha)^{13}\mathrm{N}$ reaction or from ^{13}C (rare isotope of carbon, 1 % abundance) by (p,n) reaction. As low-energy proton-induced nuclear reactions have generally been extensively studied no further demonstrations of the different reactions were felt necessary.

4.4.2 Initial spectral measurements

Spectral measurements were initially carried out only in the plasma blow-off direction. At this time thick glass targets (0.5–1.5 mm thick) were used and no ion transmission through the target was expected. These stacks consisted of twelve 12 μm foils, backed by two 100 μm foils and one 250 μm foil. Qualitatively the response of this stack is close to that shown in Figure 4.3. The sensitivity in the thin front foils is relatively low but they provide high-resolution information about the low energy ions just barely above the activation threshold. The thick foils at bottom have higher sensitivity to provide some rough information about the high-energy ions.

Typically the measured activity decreased rapidly in the first thin foils and much less activation was measured in the foils deep in the stack (Fig. 4.5). This is an indication of a rapid decrease in the ion spectrum just above the activation thresholds. To estimate the incident ion spectrum the activation response of the stack was simulated by MATLAB using a quasi-thermal model and searching for the best fit to the measured activation by varying the temperature. Typically nearly perfect fits were obtained using this method with temperatures ranging from 1 to 2 MeV.

The ion temperature fixes the activity ratios between the foils and the total incident ion flux is then proportional to the total activation yield. In these studies the activation stacks spanned only about 0.02 sr, hence they were only sampling a

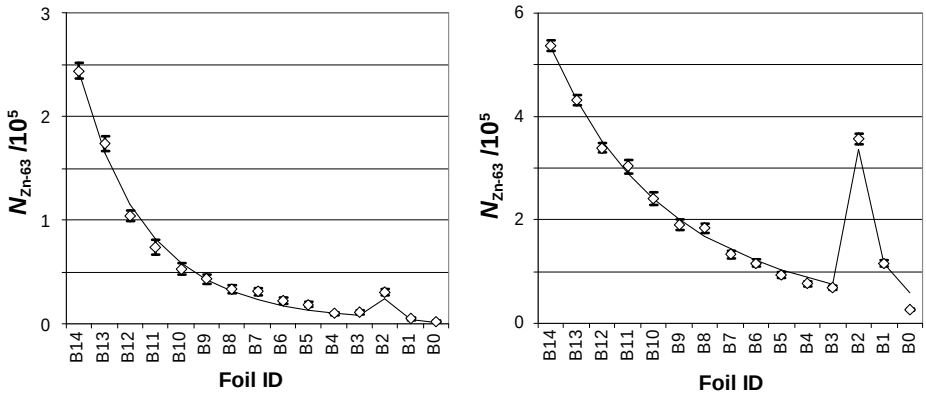

FIGURE 4.5. *Two typical examples of the measured activation response of the activation foil stacks (with 12 μm front foils). The diamonds indicate the measured activation and the solid line is the best exponential fit to spectrum. The best-fit temperatures are 1 and 2 MeV. The large activation in foils B0–B2 is due to their large thickness.*

part of the total ion emission. The number or protons above 5 MeV incident on the stacks was typically between 10^9 and 2×10^{10} corresponding to ion fluence up to 6×10^{11} sr^{-1}.

4.4.3 Ion emission in blow-off and transmitted directions

In a later experiment the ion emission was studied simultaneously both in front of the target (blow-off ions) and behind the target (transmitted ions). For this study, thin metal foils were used as targets so that ions can traverse through the targets without too much slowing down. The activation stacks described in Figure 4.3 were used and they were placed close enough to the target so that essentially all the ions impinged on their front surface. This way the activation results can be more directly related to the absolute number of ions.

The increase in ion fluence had sometimes the undesired result that the topmost foils were partially damaged by melting. The damage patterns also give confidence that most ions were collected by the stack. This is further reinforced by observation of similar patterns by other ion diagnostics like radiochromic film (RCF) and CR-39 [65, 67]. The damage affected only the topmost layers, which could indicate that it was mainly due to the heavy ions (they are quickly stopped in solids). The total activity in the stacks increased by an order of magnitude from the initial study and normally tens of kBq were measured in a single stack. Because of the increased activity the counting was delayed to reduce the exposure to the open positron-emitting samples.

The measured activation profiles indicated that the blow-off ions had a reasonably quasi-thermal spectrum but the quasi-thermal model could not explain the transmitted spectra. The activation profiles were unfolded into spectral bins (as in Ref. [Publ5]) or fitted with a multiparameter model. A model with two linear sections with a variable middle-point and end-point (three free parameters) produced generally satisfactory results as can be seen in Figure 4.6.

The most important observation in this experiment is that the spectrum of the

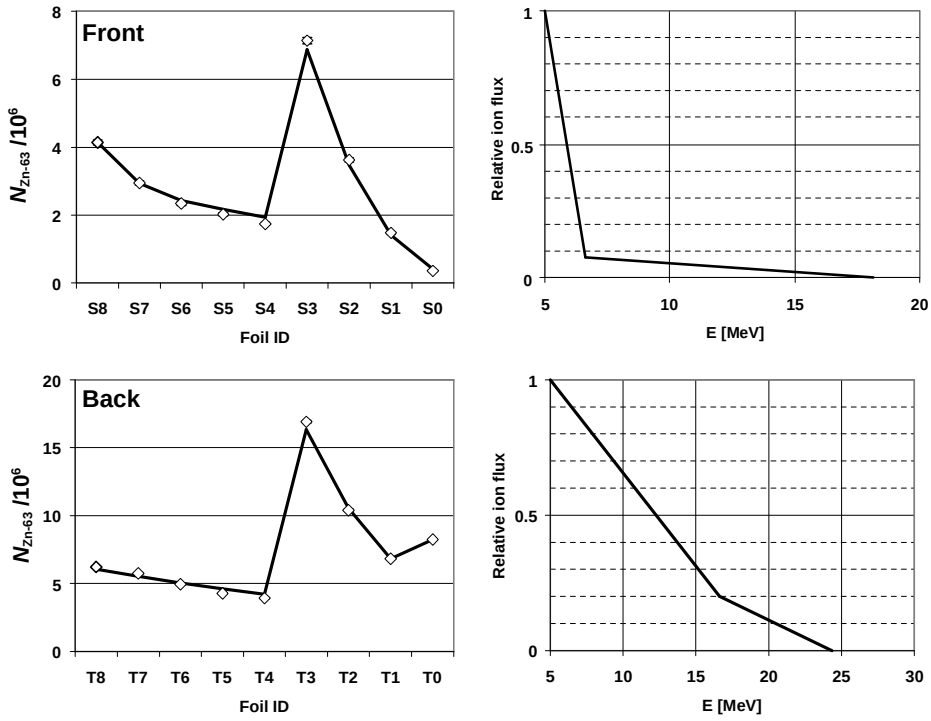

FIGURE 4.6. *Sample activation profiles measured on a single shot (left column), top row in front and bottom row behind the target. Stacks with 20 μm front foils were employed. The diamonds indicate the measured activation and the solid line is the best fit with a two-section piecewise linear fit (shown in right column).*

transmitted ions is much harder than that of the ions in blow-off. This is clearly seen in the two distributions shown in Figure 4.6. Typically, the total number of protons (above 5 MeV) is found to be similar in both directions but there is much more activation by the transmitted ions (Fig. 4.7). This can be explained by the fact that the energetic protons are much more penetrating and more likely to induce activation (see Fig. 4.3) than the ones just exceeding the threshold.

The fact that the blow-off ions have a large soft component is clearly demonstrated by the large differences measured in the activation of the first thin foils. The activation threshold is increased by about 0.5 MeV in each foil in the stack. Despite the small difference in threshold energy, a factor of 2 to 4 difference is usually observed in the activation between the topmost and the fifth foil in the stack. For the transmitted spectra, the corresponding ratio was 1.5 to 2, consistent with a much harder spectrum.

Shot-to-shot variations in the activity were larger (about a factor of five) than the variation in laser power (less than a factor of two) in successful shots. This can be compared to the electron measurements, where about two orders of magnitude variations were observed with similar laser variations. The lesser variation can largely be explained by the fact the photonuclear diagnostic is operating close to the

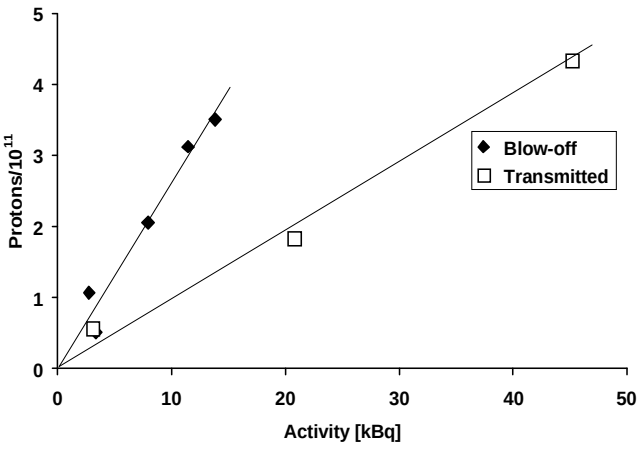

FIGURE 4.7. *The estimated number of protons (E >5 MeV) in the blow-off and transmitted direction as function of the total measured activity in the stacks. The data points follow a linear dependence indicating that shot-to-shot variations in spectral shape are small.*

threshold but the protons are well above threshold energy. The proton production is presumably sensitive to the surface condition as their origin is likely to be surface contamination, at least in the case of non-hydrogenous targets.

The mechanisms accelerating the ions are still under study. For the blow-off plasma, a large part of acceleration can result from space-charge effects during plasma expansion. This is particularly likely for the lower energy ions. Phenomena occurring near the critical surface are likely to create the faster ions [65].

For the transmitted ions there is even some confusion over whether they originate front or back of the target [25, 35, 65, 75]. These experiments support the view that the origin of ions is at the front, close to the critical surface. This is evidenced by the observation of a magnetically-induced ring structure of the transmitted ions [35] as well as by heavy ion results (see the next paragraph and Ref. [76]). Ponderomotive acceleration (charge separation) appears to be the most likely mechanism generating fast ions. Plasma waves and electric fields generated by the large currents of fast electrons can also contribute [65].

4.4.4 Heavy ion reactions

To study heavy ion reactions, some activation stacks were covered by 10–20 μm of Al foil. The exposed foils were analysed by a Ge detector to detect any induced activity. Peaks corresponding to ^{34m}Cl and ^{38}K were found and these were observed to decay in accordance with the corresponding half-lives (Fig. 4.8). The presence of ^{38}K was unanticipated, but it can be produced in reaction ^{27}Al(^{12}C,n)^{38}K. Heavy ion products were observed only in the topmost foils, ruling out their production by (γ, n) reactions in possible traces of KCl on the foils. Activation was observed with aluminium and glass targets.

No γ-rays peaks corresponding to heavy ion reactions were observed if the topmost foils were copper. This shows that the activation is produced in the exposed foil

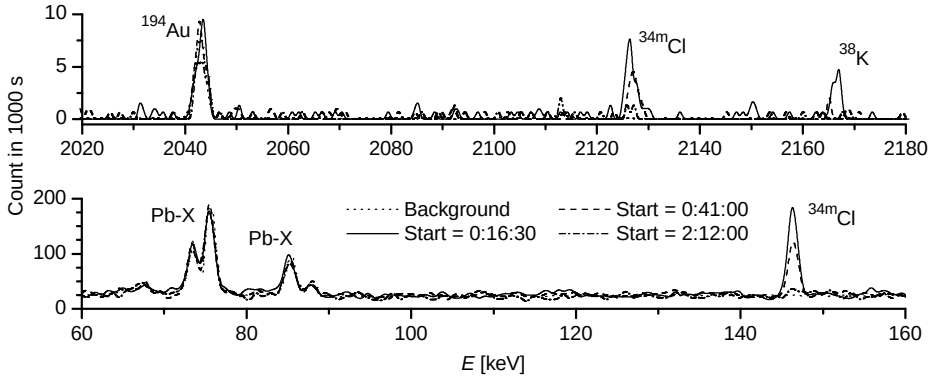

FIGURE 4.8. *Gamma spectra measured in aluminium foils exposed to plasma blow-off with 1000 s counting time at three different times after shot. 146 keV and 2128 keV lines of ^{34m}Cl ($T_{1/2}$=32.0 min) and 2167 keV line of ^{38}K ($T_{1/2}$=7.6 min) are clearly observed. The signal strength of these is observed to decay in the later spectra while background lines remain intact.*

and not within the primary target. Hence, the most plausible explanation for the activation is that the fast ^{12}C ions in the blow-off interact with ^{27}Al nuclei in the exposed foil.

The heavy ion activation products were commonly observed only in the plasma blow-off direction but never in the transmitted direction. This suggests that ions predominantly originate at the front of target and the heavy ions are stopped within target. These conclusions are consistent with the other observations in the VULCAN experiments [35, 65] but not with the LLNL experiments where ions are believed to originate from the back surface of target [25].

4.5 Comments on the ion measurements

Ion-induced nuclear reactions must be taken into account in ultra-intense laser-solid experiments even when one is not applying them as a diagnostic. As large quantities of ions with multi-MeV energies are produced by the plasma, nuclear reactions can and do occur regardless of whether they are used as a diagnostic or not. Two potential hazards need to be considered: induced radioactivity in materials exposed to plasma and fast neutrons from the (p, n) reactions.

Activation can be particularly hazardous, as it is located close to surface. This allows a large part of positrons to escape leading to potentially high dose rates on contact with exposed materials. Many plastics are especially vulnerable as the low-Z compounds have long proton stopping ranges but can still have large reaction cross-sections. For the copper foil stacks in of this work, the dose rate on contact can be estimated to reach several mSv/h. Fast neutrons can also be of a significant concern. They are produced in any (p, n) reactions, including the ones with stable products. Often such reactions have lower thresholds than the ones with highly active products. Most vulnerable for neutron-production are low-Z materials, especially lithium. Fast neutrons are much more penetrating than ions and can thus escape experimental chambers unhindered unless neutron shielding is employed. Unfor-

tunately, hydrogen-bearing materials like biological tissue are the most efficient in stopping fast neutrons, yet fast neutrons are among the most damaging types of radiation [77].

The large activation yields observed in the experiments open up the possibility of using intense laser-solid interactions for production of short-lived radioactive sources for practical applications [78, Publ5]. The spectral distribution of ions is believed to be approximately proportional to the focussed laser intensity [67]. The emerging table-top laser systems with pulselength close to 20 fs are able to reach similar intensity as the Vulcan laser at a high repetition rate [14, 15]. Hence, it appears to be plausible to accumulate the activity for many shots to achieve large activities.

This technique is likely to be most feasible in the production of short-lived proton-rich nuclides that are presently made with ion cyclotrons. Production of ^{11}C, ^{13}N, ^{15}O and ^{18}F for positron emission tomography (PET) could be a possible application. In [Publ5] it has been estimated that even an 1 J-per-pulse laser operating at 10 Hz could be sufficient to produce enough activity ($>$ 100 MBq) for PET uses.

CHAPTER 5

Electron plasma accelerator

Underdense plasma accelerators are compact sources of energetic electrons. They commonly operate in nearly homogeneous plasmas with much lower electron density than in the laser-solid interaction. Typically the density is not more than a few per cent of the critical density (a few times 10^{19} cm^{-3}). Most commonly such accelerators are realised by focussing an intense laser beam to the edge of a pulsed gasjet in vacuum.

The laser fields are coupled to the electrostatic plasma waves through nonlinear processes like ponderomotive force. Unlike the light wave with a transverse electric field the electrostatic oscillations have the electric field in the direction of propagation. Furthermore, such modes can have phase velocity close to the speed of light in warm plasmas. This has two important consequences: the plasma wave can nearly co-propagate with the laser beam and a relativistic particle co-propagating in the wave (trapped particle) can experience a continuous acceleration over a long distance. Furthermore, relativistic self-focusing [79, 80] channels the laser beam into one or more non-diverging narrow filaments greatly increasing the intensity of the laser beam and increasing the interaction distance up to several millimetres [70, 80]. As the accelerating field can exceed 100 GV/m, electrons up to 100 MeV have been observed from such particle accelerators [81, Publ6].

There are several methods to excite the plasma wave. The most studied one is the self-modulated laser wakefield accelerator (SM-LWFA), where stimulated Raman scattering couples the laser fields and the plasma wave (see Ref. [18] for an excellent review of plasma acceleration mechanisms). The photons in laser beam lose an amount of energy corresponding approximately to the plasma frequency ω_p, which results in a corresponding frequency shift in the laser beam. In the case of Raman forward scattering the frequency and wave vector matching conditions result in the excitation of plasma waves having the phase velocity close to the speed of light. Scattering may occur multiple times and as the plasma wave becomes stronger, the inverse process may also occur. Hence, the initially monochromatic laser beam will consist of multiple additional lines, spaced at the plasma frequency [82, 83]. This mechanism can be sufficiently strong to reach wavebreaking [17, 82], resulting in an efficient electron acceleration. Wavebreaking can also greatly enhance the electron trapping into the plasma wave.

Another, more recent scheme recently identified in computer simulations [47] and observed experimentally [84] is the direct laser acceleration (DLA). The net acceleration of electrons occurs through betatron oscillations of the electrons in the laser channel. This mechanism results in electron acceleration without a plasma wave. It is predicted to be the dominant acceleration method in fairly dense, inhomogeneous plasmas and at moderate laser powers. However, it can contribute to electron acceleration also at lower densities and high laser powers.

5.1 Measuring the electron beam properties

It is important to know the properties of the accelerated electron beam both for understanding the acceleration process and for potential practical applications. The beam needs to be characterised in terms of energy spectrum, divergence and the total number of electrons accelerated. It is also important to find out how these properties vary under different experimental conditions.

In previous work, the electron spectra have typically been measured by small-aperture electron spectrometers [81, 82, 83, 85, 86, 87]. In some cases, the angular dependence of the beam has been measured by rotating a compact spectrometer and averaging the spectrum over many laser shots [84] or by exposing film through absorbers of different thickness [49, 88]. The divergence has been measured by exposing either a film or a scintillating or fluorescent screen to the electrons, possibly through some energy filter layers [49, 83, 88, 87]. The divergence measurements have also been used to estimate the total electron yields.

The principal concern in these measurements is that the bremsstrahlung X-rays can affect the results. Detectors are integrating the deposited energy, and it is generally impossible to differentiate signal from electrons and X-rays. Being more penetrating than electrons, X-rays can skew the spectral filtering. The problems with X-rays are small at low energies (< 1 MeV) where few X-rays are generated in low-Z materials. However, the most intense plasma accelerators produce large quantities of electrons at tens of MeV, and such electrons generate hard X-rays effectively in any material. Shielding is difficult because high-Z materials that are the most efficient in attenuating X-rays also are the most efficient in generating them. In addition, the range of electrons at these energies can be substantial (> 10 cm for low-Z materials).

Resolving the energy spectrum at high energies can only be done by magnetic spectrometers. Their drawback is that they typically have a very small acceptance angle, f-numbers in the range 50–100 being typical. Consequently, they measure only a small portion of all the accelerated electrons. Involving magnets of heavy construction, they are also susceptible to the hard X-ray background problems.

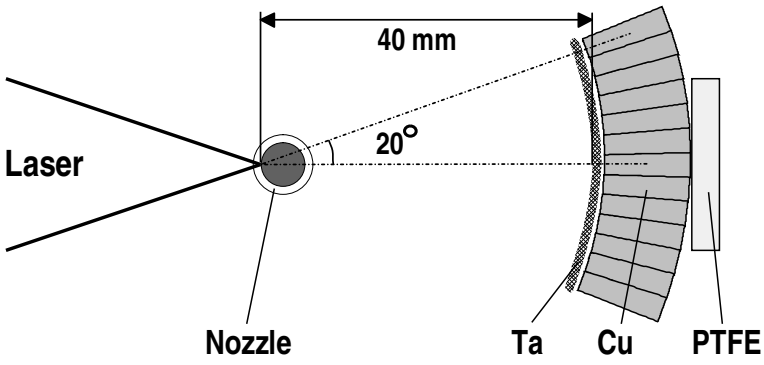

FIGURE 5.1. *Schematic view of the setup in the gasjet experiments. Laser beam interacts with the gasjet produced by the nozzle. Bremsstrahlung is generated by the accelerated electrons in the Ta layer, and it activates the Cu and* PTFE *pieces. [Publ6]*

TABLE 5.1. *Nuclear reaction pairs used. Q is the reaction threshold, $\sigma_{\max}$ is the peak cross-section, $T_{1/2}$ is the half-live of the reaction product and γ-rays are the main radiation energies [52, 63].*

Reaction	Q [MeV]	$\sigma_{\max}$ [mb]	Decay	$T_{1/2}$	γ-rays [keV]
^{63}Cu$(\gamma,n)^{62}$Cu	10.9	75	β^+	9.7m	—
^{63}Cu$(\gamma,2n)^{61}$Cu	19.7	13	β^+	3.3h	283, 656
^{181}Ta$(\gamma,n)^{180}$Ta	7.6	350	EC,β^-	8.2h	93, 104
^{181}Ta$(\gamma,3n)^{178}$Ta	22.1	20	EC	2.4h	213, 326, 426
^{12}C$(\gamma,n)^{11}$C	18.7	9	β^+	20m	—
^{19}F$(\gamma,n)^{18}$F	10.5	10	β^+	110m	—

5.2 The photo-nuclear diagnostic

In this work many of the shortcomings of the other diagnostics have been addressed by the application of the photo-nuclear techniques to the characterisation of the electron beam. In effect, this diagnostic turns the hard X-ray background into an advantage. It derives the properties of the electrons from the properties of bremsstrahlung. Due to the reaction thresholds exceeding 10 MeV, the diagnostic is only sensitive to electrons with meaningful high energies. This diagnostic is used to measure the electron beam divergence, to measure "effective" temperature and to estimate the total yield of the electrons. These are essentially measured over full-beam. The principal aim was to measure the parameters as a function of plasma density. In addition, some measurements were done at a constant density but the laser power was varied.

In the experimental arrangement (Figure 5.1), the laser beam is focused to the front edge of the helium gasjet. The gasjet has a very homogeneous density profile resulting in a very homogeneous plasma density [89]. Fast electrons are generated in the plasma, and the most energetic ones are travelling along the direction of the laser beam. These electrons first enter a 1 mm thick layer of tantalum to maximise the production of energetic bremsstrahlung. The tantalum layer is not sufficient to stop the electrons so they next enter the copper where bremsstrahlung is also generated but at a reduced intensity and energy.

The main activator material, copper, is segmented into 13 pieces at approximately 3-degree spacing. Bremsstrahlung is generated along the direction of propagation of the incident electrons. Hence, each copper piece is subjected to bremsstrahlung flux that corresponds to the electron flux in that direction. The activation distribution is thus correlated with the incident electron distribution and it is directly proportional to the electron flux if the electron spectrum is not dependent on the angle.

5.2.1 Spectral diagnostic

The electron spectrum can be deduced by studying several different activation reactions simultaneously. As different reactions have different energy–cross-section dependencies the ratios of the yields from different reactions depend on the incident electron energy spectrum. By measuring the yield of two reactions it is possible to find out one parameter defining the spectral shape and the total number of incident particles. By measuring more reactions it is possible to define more complicated spectral models.

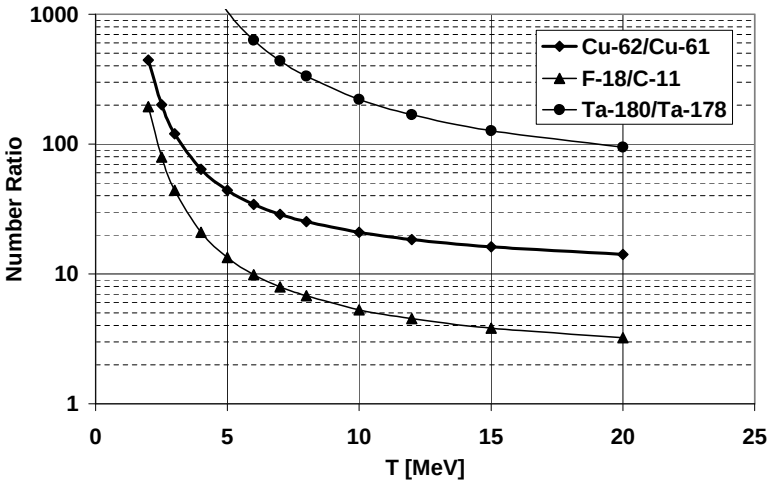

FIGURE 5.2. *The reaction yield ratios from different reaction pairs as a function of electron temperature. These correlations are calculated by folding the simulated bremsstrahlung spectra with the activation cross-sections.*

In this work, a simple quasi-thermal model $f(E) = f_0 \exp(-E/kT)$ was used. Here $f(E)$ is number density of electrons at energy E, f_0 is a scaling parameter proportional to the total number of electrons and T is the temperature, *i.e.* the parameter defining the spectral shape. This is a reasonable assumption as seen in magnetic spectrometer measurements [81, 84, Publ6] as well as in several *particle-in-cell* (PIC) simulations [47]. This model was applied separately to reaction pairs in copper, tantalum and PTFE (polytetrafluoroethylene). The studied reaction pairs are shown in Table 5.1.

The slowing-down of the electrons and the generation of bremsstrahlung were modelled numerically in order to correlate the observed activation yields with the number of electrons and their temperature. The total and radiative energy loss were modelled by data from ESTAR database [60]. The bremsstrahlung spectrum at the instantaneous energy of the slowing-down electron was modelled using data by Seltzer and Berger [58]. The calculated bremsstrahlung spectrum was folded with the reaction cross-sections [52] to estimate the activation yield of each reaction at different "effective" temperatures T. The yield ratios for the studied reaction pairs are shown in Fig. 5.2. Once the temperature has been determined, the total electron yield is proportional to the absolute activation yields.

5.3 Experimental results

The ^{62}Cu activity in each copper segment was measured and corrected for decay. The data was fitted with Gaussian model to determine the width of the electron beam. It was clearly observed that the electrons were emitted in a fairly wide cone instead of a narrow beam, and the opening angle of the cone increases with the plasma density (Fig. 5.3).

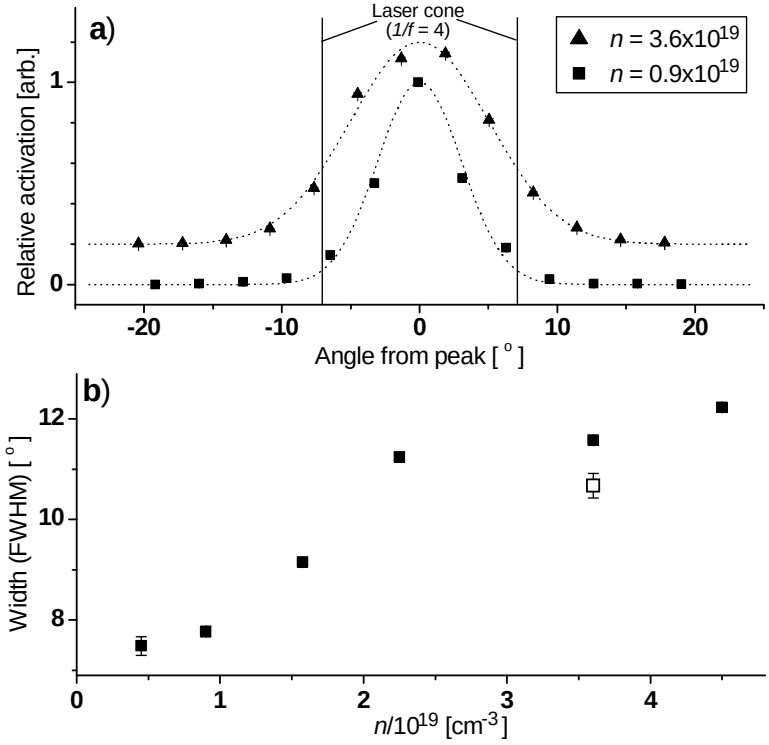

FIGURE 5.3. *Measured angular distributions at a low and high density (a) and dependence of the angular width (FWHM) on the plasma density (b). The open square denotes a low-power shot. [Publ6]*

Energy dependence of the angular distribution could be determined by measuring also the ^{61}Cu activity. Unfortunately, this activity was generally too low to allow an accurate segmentwise measurement. Instead, a rough measurement was carried out at some of the high-yield shots by measuring ^{61}Cu activity in a few central segments and in segments surrounding these. The ratio of activity in the 'central set' to the 'surrounding set' was compared to a corresponding ratio from the ^{62}Cu measurements. No significant difference was found in the ratios, which indicates that the energy spectrum is not highly energy dependent. This justifies the use of only ^{62}Cu activation in the angular distribution measurement.

For the determination of the electron temperature and yield, the activities of the reaction pairs in Table 5.1 were determined (Figure 5.4a). On shots with a large activation yield the temperatures were on average 8.2 MeV in copper, 10.8 MeV in PTFE, but only 4.4 MeV in tantalum. The good agreement between copper and PTFE measurements is good evidence to that the electron spectrum is approximately exponential. The discrepancy between tantalum and the others results probably from the difficulty in measuring the activation accurately: the source distribution is highly uneven and self-absorption effects are large and difficult to compensate for. It is remarkable that the ^{181}Ta$(\gamma, 3n)^{178}$Ta reaction was observed at all despite its small cross-section that peaks at 25–30 MeV.

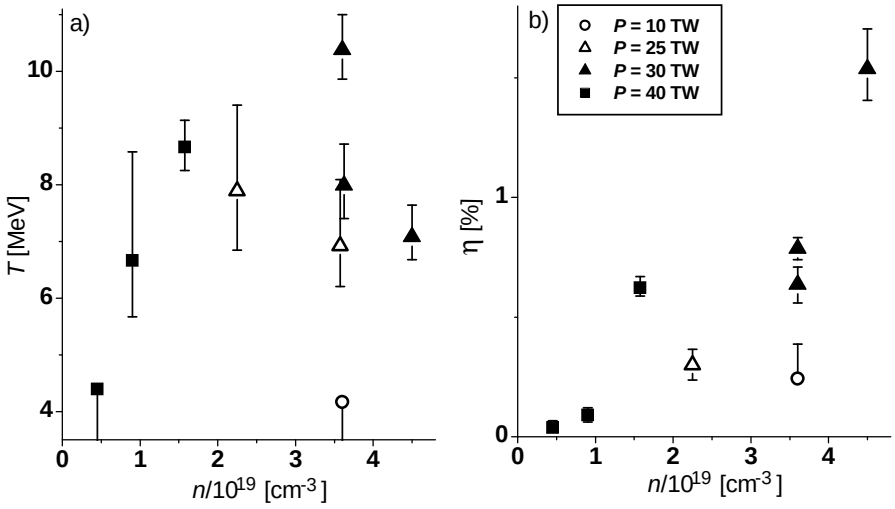

FIGURE 5.4. *(a) Measured (Cu activation) temperatures at different plasma densities and laser powers. (b) Energy conversion efficiency from laser energy to electrons above 10 MeV. [Publ6]*

The number of accelerated electrons was estimated with the quasi-thermal model using the copper data. In shots with a large activation yield, the number of electrons above 10 MeV was $1.5 - 3.8 \times 10^{11}$ and the lowest yields were close to 10^{10}. To reasonably explain the largest ^{178}Ta activation, 10^9–10^{10} electrons must be above 40 MeV.

The total energy carried by the (>10 MeV) electrons is estimated to be up to 1 J, corresponding to a conversion efficiency of 2 %. It is plotted as a function of plasma density in Figure 5.4b. An increasing dependence is clearly observed. This would suggest that the laser fields are more efficiently coupled into plasma waves as density increases, and furthermore, the plasma fields are more efficiently loaded. In principle, a poor efficiency is expected at low-densities as complete cavitation of the high-intensity region may occur [80].

As the electrons are presumably accelerated in a bunch with 1-ps duration [90, 91] they carry a very large current. For electrons above 10 MeV the current is up to 60 kA. If the quasithermal model is assumed to hold also at lower energies the total beam current would be about 200 kA (T = 8 MeV). This is fairly close to the Alfvén limit (350 kA at 10 MeV) where the self-induced magnetic field limits the current propagation. Hence, it is likely that the self-induced magnetic fields can affect the propagation of the electrons, particularly at low energies. Plasma-lensing like phenomena [92] may be contributing to the observed beam divergence.

5.4 Comments on plasma accelerators

It is interesting to compare the electron spectra in the laser-solid interaction to the underdense plasma accelerator with similar laser parameters. In the plasma accelerator case typically 8–10 MeV was measured but 1–2 MeV was typical in the

laser-solid interaction. This difference likely arises from the fact that few dominant, ordered acceleration mechanisms are acting over a long distance in a nearly homogeneous plasma in the plasma accelerator. In laser-solid interaction, most electron acceleration occurs in the very inhomogeneous, small plasma close to the critical surface. There are numerous mechanisms acting in regions close to each other, and because of the large density, there are always many electrons available to load the fields formed. This leads to a high efficiency in converting light energy into electron kinetic energy (after all, laser beam is abruptly stopped and the light momentum must go somewhere). However, on average, electrons gain less energy than in the in the underdense accelerator. If the laser-solid interaction takes place with an order of magnitude higher laser intensity it can reach similar electron temperature as the present underdense accelerator [51].

The very high temperatures we observe could, in principle, be explained by ponderomotive acceleration alone if the laser beam self-focussed strongly enough. A focused intensity of 10^{21} W/cm^2 would be needed to reach such a temperature [51]. Such self-focusing is actually predicted in some 2D simulations [93]. However, 2D simulations are not sufficient to resolve all the relevant physics. More detailed 3D simulations show that as the laser power is increased the beam breaks into multiple filaments and a much smaller peak intensity is obtained [80]. This has also been confirmed experimentally by Thomson scattering [80] and by measuring radially ejected ions [70]. The latter measurement was carried out with the same laser as the activation measurements and showed a maximum intensity enhancement by a factor of six over the vacuum intensity.

Even though fewer relativistic electrons are produced by the plasma accelerator than in the laser-solid interaction, they are typically much more relativistic. This results in an efficient generation of energetic bremsstrahlung, which leads to comparatively large activation yields. Typically 10–20 kBq of ^{62}Cu activity was produced in the gasjet experiment while less than 1 kBq was typically observed in the laser-solid experiments. The number of activated nuclei produced (typically $1 - 2 \times 10^7$) and the electron temperatures are actually very close to laser-solid experiments carried out at an order of magnitude larger laser intensity [51]. Hence, the electron spectra in laser-solid experiments are reasonably consistent with ponderomotive acceleration mechanisms while more complicated acceleration mechanisms are necessary to explain the electron spectra in the underdense experiments.

CHAPTER 6

Conclusions

In this thesis the use of nuclear activation techniques in the diagnosis of intense laser-plasma interactions has been studied. Two different approaches have been applied: photoneutron reactions to study the bremsstrahlung generated by the fast electrons produced in the interaction and ion-induced nuclear reactions to study energetic ions ejected from the plasma. In laser-solid experiments, photoneutron activation has been applied to the measurement of the direction of energetic electrons and how this direction depends on the amount of pre-ionised plasma on the solid surface. The energetic ion emission has been quantitatively characterised by ion-induced activation. In experiments on underdense plasma accelerators, the energetic electron beam has been characterised in terms of spectrum (temperature), divergence and electron yield. These properties have been measured as a function of plasma density.

The most appealing property in the nuclear diagnostics is the high reaction thresholds of many MeVs. Hence, activation removes the ambiguity between single high-energy particle and multiple low energy ones and so provides conclusive evidence of the presence of very energetic particles. By using several reactions simultaneously, the nuclear diagnostic can provide energy selectivity also at the large photon energies where conventional diagnostics capable of high-flux operation have little if any selectivity left. Another remarkable advantage is that the photonuclear technique allows an *in situ* diagnosis of the fast electrons in laser-solid experiments because bremsstrahlung can be generated within the target structure. This is in contrast to many other diagnostics that must be placed away from the target making the measurements vulnerable to space-charge effects. Other advantages include potential for large solid angles of detection allowing 'full-beam' measurements, insensitivity to electronic disturbances due to off-line data analysis and the wide dynamic range achievable. Also the relatively low sensitivity is well suited for the laser-plasma experiments where very large instantaneous particle fluxes are generated.

The analysis of bremsstrahlung is important as it allows one to deduce information about the fast electrons generated in the laser-plasma interaction. Because the interaction occurs primarily between laser light and the plasma electrons the accelerated electrons convey most information about the interaction physics. The photonuclear activation techniques are particularly applicable to electrons with energies in the range from 10 MeV to about 50 MeV as there are numerous strong reactions with well-known cross-sections. The main drawback of the method is the large degree of averaging due to the facts that bremsstrahlung has a wide spectrum and that the reaction cross-sections are significant over large energy bands. Hence, in spectral measurements, it is only possible to deduce large-scale features like effective electron temperature.

In the laser-solid experiments, it has been demonstrated that photonuclear reactions can be induced in laser-solid experiments at a moderate-energy (about 50 J) laser with a focused intensity up to 2×10^{19} W/cm^2. Coincidence counting has been

extensively applied to the detection of minute amounts of activation. In the work, several different nuclear reactions including photo-fission have been demonstrated [Publ3]. Based on these and other bremsstrahlung measurements the effective electron temperature was estimated to be 1–2 MeV.

The technique was applied primarily in the study of the directionality of the fast electrons [Publ1, Publ2]. In particular, the dependence of the direction of accelerated electrons on the amount of pre-plasma was studied. In the case of small pre-plasma, the electrons were found along the direction of target normal but as the pre-plasma was made larger, the electrons were mainly found in the direction of the laser beam. This would suggest a change in the predominant acceleration mechanism from Brunel-like mechanisms to ponderomotive acceleration. If the pre-plasma was made very large, an uncorrelated behaviour was observed. This could result from beam propagation instabilities in the large, inhomogeneous plasma.

The laser-solid interactions are known to produce energetic ion jets in addition to the fast electrons. In this work, ion-induced nuclear reactions were applied to study these ions [Publ4, Publ5]. The total proton yields and spectra were determined by the use of stacked foil detectors. As less averaging occurs than in the photonuclear technique, more accurate spectral information can be obtained by unfolding techniques. The numbers of protons accelerated were found to be similar both in front of the target and behind the target. However, much more energetic spectra were seen behind the target. In addition to proton-induced reactions, evidence of nuclear reactions induced by carbon ions was also obtained. Carbon reactions were seen only in the front of the target, never behind. This suggests that ions are accelerated at the front surface of the target.

The photonuclear technique was also applied in the study of underdense laser-driven plasma accelerators, *i.e.* gasjet experiments [Publ6]. The divergence of the electron beam, the effective electron temperature and the total electron yield were determined by this technique at different plasma densities. It was shown that the electrons are emitted in a fairly wide cone with the divergence increasing with plasma density. Quite remarkably, electron temperature and activation yield similar to those measured in laser-solid experiments with an order of magnitude more powerful lasers were observed. Due to the electron temperature approaching 10 MeV the photonuclear activation yield exceeded that of our laser-solid experiments by more than an order of magnitude.

The scope of this work is principally on the use of nuclear activation techniques in diagnosing laser-plasma interactions. However, it is of interest to note that the ultra-intense laser-plasma interactions are a previously unknown technique for production of radioactive substances. Even though the amount of activity produced in the present experiments is relatively minute, the method could still have some practical applications. First of all, many traditional sources of activated materials (research reactors, cyclotrons) are shut down. Secondly, the laser-plasma interaction physics is expected to largely scale with laser intensity. Hence, it should be possible to reach similar physical conditions with a smaller laser producing pulses of shorter pulselength and less energy. Such lasers can be operated at a high repetition rate, making it feasible to accumulate the activity for long times. Of the presently studied techniques the proton-induced activation in laser-solid interactions and photonuclear activation by an underdense accelerator appear particularly promising.

Bibliography

[Publ1] P. Norreys *et al.*, Phys. Plasmas **6**, 2150 (1999).

[Publ2] M. I. K. Santala *et al.*, Phys. Rev. Lett. **84** 1459 (2000).

[Publ3] K. W. D. Ledingham *et al.*, Phys. Rev. Lett. **84** 899 (2000).

[Publ4] M. I. K. Santala *et al.*, Inertial Fusion Sciences and Applications 99 Conference, 12-17 September 1999, Bordeaux, France. Edited by C. Labaune *et al.* Elsevier, Paris, 2000, p. 1016.

[Publ5] M. I. K. Santala *et al.*, Appl. Phys. Lett. **78** 19 (2001).

[Publ6] M. I. K. Santala *et al.*, Phys. Rev. Lett. **86** 1227 (2001).

[1] T. H. Maiman, Nature **187** 493–494 (1960).

[2] M. D. Perry and G. Mourou, Science **264** 917 (1994).

[3] M. H. Key *et al.*, Phys. Plasmas **5**, 1966 (1998).

[4] Central Laser Facility web site at http://www.clf.rl.ac.uk

[5] Lawrence Livermore National Laboratory Lasers web site http://lasers.llnl.gov

[6] C. Yamanaka. Laser Part. Beams **17** 145 (1999).

[7] Institute of Laser Engineering at Osaka University web site http://www.ile.osaka-u.ac.jp

[8] J. D. Kilkenny *et al.* Laser Part. Beams **17** 159 (1999).

[9] M. L. Andre, in IFSA 99, Ed. C. Labaune, Elsevier, 32 (2000).

[10] T. B. Brabec and F. Krausz, Rev. Mod. Phys. **72** 545 (2000).

[11] P. Maine *et al.* IEEE J. of Quant. El. **24** 398 (1988).

[12] C. N. Danson *et al.*, J of Mod. Opt. **45**, 1653 (1998).

[13] C. G. Durfee *et al.*, IEEE J. Quant. El. **4** 395 (1998).

[14] K. Yamagawa *et al.*, IEEE J. Quant. El. **4** 385 (1998).

[15] H. Wang *et al.*, J. Opt. Soc. Am. B **16** 1790 (1999).

[16] F. F. Chen *Introduction to plasma physics and controlled fusion*, Plenum, London (1984).

[17] W. L. Kruer *The physics of laser plasma interactions* in series Frontiers in Physics (73), Addison-Wesley, United States (1988).

[18] E. Esarey *et al.*, IEEE Trans. Plasma Sci. **24** 252 (1996).

[19] S. C. Wilks and W. L. Kruer, IEEE J. Quant. El. **33**, 1954 (1997).

[20] M. Tabak *et al.*, Phys. Plasmas **1**, 1626 (1994).

[21] G. Malka and J. L. Miquel, Phys. Rev. Lett. **77**, 75 (1996).

[22] F. N. Beg *et al.* Phys. Plasmas **4** 447 (1997).

[23] G. Malka, E. Lefevbre, and J. L. Miquel, Phys. Rev. Lett. **78**, 3314 (1997).

[24] K. B. Wharton *et al.*, Phys. Rev. Lett. **81**, 822 (1998).

[25] S. P. Hatchett *et al.*, Phys. Plasmas **7** 2076 (2000).

[26] A. Pukhov and J. Meyer-ter-Vehn, Phys. Rev. Lett **79** 2686 (1997)

[27] A. Pukhov and J. Meyer-ter-Vehn, Phys. Plasmas **5**, 1880 (1998).

[28] B. F. Lasinski *et al.*, Phys. Plasmas **6** 2041 (1999).

[29] H. Ruhl *et al.*, Phys. Rev. Lett. **82**, 743 (1999).

[30] A. Pukhov and J. Meyer-ter-Vehn, Phys. Rev. Lett. **76**, 3975 (1996).

[31] R. J. Mason and M. Tabak, Phys. Rev. Lett. **80**, 524 (1998).

[32] A. R. Bell, J. R. Davies, S. M. Guerin, Phys. Rev. E **58** 2471 (1998)

[33] J. R. Davies *et al.*, Phys. Rev. E **56** 7193 (1997).

[34] M. Tatarakis *et al.*, Phys. Rev. Lett. **81**, 999 (1998).

[35] E. L. Clark *et al.*, Phys. Rev. Lett. **84** 670 (2000).

[36] J. Zhang *et al.*, Phys. Rev. A **54** 1597 (1996).

[37] R. Lichters, J. Meyer-ter-Vehn, and A. Pukhov. Phys. Plasmas **3** 3425 (1996).

[38] D. W. Forslund *et al.* Phys. Rev. A **11** 679 (1975).

[39] K. G. Estabrook *et al.* Phys. Fluids **18** 1151 (1975).

[40] J. Albritton and P. Koch. Phys. Fluids **18** 1136 (1975).

[41] J. C. Kieffer *et al.* Phys. Rev. Lett. **62** 760 (1989).

[42] U. Teubner *et al.* Phys. Rev. Lett. **70** 794 (1993).

[43] F. Brunel, Phys. Rev. Lett. **59**, 52 (1987).

[44] P. Gibbon and A. R. Bell. Phys. Rev. Lett. **68** 1535 (1992).

[45] S. C. Wilks *et al.* Phys. Rev. Lett. **69**, 1383 (1992).

[46] T. Tajima and J. M. Dawson, Phys. Rev. Lett. **43**, 267 (1979).

[47] A. Pukhov, Z.-M. Sheng, and J. Meyer-ter-Vehn, Phys. Plasmas **6** 2847 (1999).

[48] T. Feurer *et al.*, Phys. Rev. E **56**, 4608 (1997).

[49] C. I. Moore *et al.*, Phys. Rev. E **61** 788 (2000).

[50] D. R. Goosman, *Radiographic X-ray flux monitoring during explosive experiments by copper activation* LLNL Report UCRL 93074 (preprint), LLNL (1986).

[51] T. E. Cowan *et al.*, Phys. Rev. Lett. **84** 903 (2000).

[52] EXFOR online-database at http://www-nds.iaea.org

[53] G. F. Knoll, *Radiation detection and measurement. 2nd ed.*, Wiley, (1989).

[54] B. L. Berman and S. C. Fultz, Rev. Mod. Phys **47**, 713 (1975).

[55] K. Boyer *et al.* Phys. Rev. Lett. **60** 557 (1988).

[56] T. W. Phillips *et al.* Rev. Sci. Inst **70** 1213 (1999).

[57] Jackson J. D. *Classical electrodynamics, 2. ed.* Wiley, New York (1975).

[58] S. Seltzer and M. Berger, At. Data Nucl. Data Tables **35** 345 (1986).

[59] R. K. Bock and A. Vasilescu, *The Particle Detector BriefBook*, Springer-Verlag, 1998.
Also online at http://physics.web.cern.ch/Physics/ParticleDetector/BriefBook.

[60] Estar online-database at http://physics.nist.gov

[61] CERN Program Library Long Writeup W5013.

[62] J. Davies, A. R. Bell, and M. Tatarakis, Phys. Rev. E **59** 6032 (1999).

[63] NUDAT online-database at http://www-nds.iaea.org

[64] A. P. Fews *et al.*, Phys. Rev. Lett. **79** 5258 (1997).

[65] K. Krushelnick *et al.*, Phys. Plasmas **7** 2055 (2000).

[66] P. A. Norreys *et al.*, Plasma Phys. Control. Fusion **40** 175 (1998).

[67] E. L. Clark *et al.*, Phys. Rev. Lett. **85** 1654 (2000).

[68] M. Roth *et al.*, in IFSA 99, Ed. C. Labaune, Elsevier, 1010 (2000).

[69] R. A. Snavely *et al.*, Phys. Rev. Lett. **85** 2945 (2000).

[70] K. Krushelnick *et al.*, Phys. Rev. Lett. **83** 737 (1999).

[71] SRIM-2000 (The Stopping Range of Ions in Matter) software package by J. F. Ziegler, IBM Research, Yorktown, USA.

[72] PSTAR online database at http://physics.nist.gov.

[73] I.-M. Ladenbauer-Bellis, I. L. Preiss, and C. E. Anderson. Phys. Rev. **125** 606 (1962).

[74] J. B. Natowitz, E. T. Chulik, and M. N. Namboodiri. Phys. Rev. C **6** 2133 (1972).

[75] M. H. Key *et al.*, in IFSA 99, Ed. C. Labaune, Elsevier, 392 (2000).

[76] M. Zepf *et al.*, (unpublished).

[77] J. R. Lamarsh, *Introduction to nuclear engineering, 2nd Edition*, Addison-Wesley, Reading, USA, 1983.

[78] M. Yamagiwa and J. Koga, J. Phys. D **32** 2526 (1999).

[79] C. E. Max, J. Arons, and A. B. Langdon, Phys. Rev. Lett. **33**, 209 (1974).

[80] A. Chiron *et al.*, Phys. Plasmas **3** 1373 (1996).

[81] D. Gordon *et al.*, Phys. Rev. Lett. **80** 2133 (1998).

[82] A. Modena *et al.*, Nature **377** 606 (1995).

[83] D. Umstadter *et al.*, Science **273** 472 (1996).

[84] C. Gahn *et al.* Phys. Rev. Lett. **83** 4772 (1999).

[85] A. Modena *et al.*, IEEE Trans. Plasma Sci. **24** 289 (1996).

[86] C . E. Clayton *et al.*, Phys. Rev. Lett. **81** 100 (1998).

[87] C. I. Moore *et al.*, Phys. Rev. Lett. **79** 3909 (1997).

[88] R. Wagner *et al.*, Phys. Rev. Lett **78** 3125 (1997).

[89] V. Malka *et al.*, Rev. Sci. Inst. **71**, 2329 (2000).

[90] A. Ting *et al.*, Phys. Rev. Lett. **77** 5377 (1996).

[91] S. P. Le Blanc *et al.* Phys. Rev. Lett. **77** 5381 (1996).

[92] J. J. Su *et al.*, Phys. Rev. A **41** 3321 (1990).

[93] A. B. Borisov *et al.*, Plasma Phys. Control. Fusion **37** 569 (1995).

Abstracts of publications I-VI

I. Novel measurements of electromagnetic radiation above 10 MeV are presented for ultra intense laser pulse interactions with solids. A bright, highly directional source of γ-rays was observed directly behind the target. The γ-rays were produced by bremsstrahlung radiation from energetic electrons generated during the interaction. They were measured using the photoneutron reaction [^{63}Cu$(\gamma, n)^{62}$Cu] in copper. The resulting activity was measured by coincidence counting the positron annihilation grays which were produced from the decay of ^{62}Cu. New measurements of the bremsstrahlung radiation at 10^{19} Wcm^{-2} are also presented.

II. The angular distribution of bremsstrahlung γ-rays produced by fast electrons accelerated in relativistic laser-solid interaction has been studied by photoneutron activation in copper. We show that the γ-ray beam moves from the target normal to the direction of the $\mathbf{k}_{\text{laser}}$ vector as the scale length is increased. Similar behavior is found also in 2D particle-in-cell simulations.

III. When a laser pulse of intensity 10^{19} Wcm^{-2} interacts with solid targets, electrons of energies of some tens of MeV are produced. In a tantalum target, the electrons generate an intense highly directional γ-ray beam that can be used to carry out photonuclear reactions. The isotopes ^{11}C, ^{38}K, ^{62,64}Cu, ^{63}Zn, ^{106}Ag, ^{140}Pr, and ^{180}Ta have been produced by (γ, n) reactions using the VULCAN laser beam. In addition, laser-induced nuclear fission in ^{238}U has been demonstrated, a process which was theoretically predicted at such laser intensities more than ten years ago. The ratio of the ^{11}C and the ^{62}Cu β^+ activities yields shot-by-shot temperatures of the suprathermal electrons at laser intensities of $\sim 10^{19}$ Wcm^{-2}.

IV. We present results from an experiment where nuclear activation has been observed in materials exposed to plasma blow-off from relativistic laser-solid interactions. The activation is caused by large numbers of protons with energies up to 20 MeV present in the plasma blow-off. The activation has been applied as a low-background diagnostic for characterisation of the number of protons and their energy spectrum in the ablated plasma. Results are found to be in agreement with other ion diagnostics.

V. Nuclear activation has been observed in materials exposed to the ablated plasma generated from high intensity laser–solid interactions (at focused intensities up to 2×10^{19} W/cm^2) and is produced by protons having energies up to 30 MeV. The energy spectrum of the protons is determined from these activation measurements and is found to be consistent with other ion diagnostics. The possible development of this technique for "table-top" production of radionuclides for medical applications is also discussed.

VI. A highly relativistic electron beam produced by a 50 TW laser-plasma accelerator has been characterized by photonuclear techniques. The beam has large divergence that increases with plasma density. The electron yield also increases with plasma density and reaches up to 4×10^{11} electrons (> 10 MeV), with beam current approaching the Alfvén limit. Effective electron temperatures exceeding 8 MeV are found, leading to an order of magnitude higher photonuclear activation yield than in solid target experiments with the same laser system.